Dinoop Lal S. "Photodegradation of polystyrene by nano titanium dioxide and photosensitizers." Thesis. Research & Postgraduate Department of Chemistry, St. Thomas' College (Autonomous), Thrissur, University of Calicut, 2020.

Chapter 5

Accelerated Photodegradation of Polystyrene using TiO$_2$ and ZnO Surface Modified with Graphene oxide

Abstract

Graphene oxide (GO) was prepared from graphite using modified Hummer's method. TiO$_2$-GO and ZnO-GO composites were developed using sonication assisted hydrothermal method. Composites of TiO$_2$-GO and ZnO-GO with 3, 10 and 30 percentages of GO were prepared. The crystal morphology of TiO$_2$ and ZnO remained unaltered upon GO coupling as evident through XRD analysis. XRD, Raman spectroscopy and XPS analysis confirmed partial reduction of GO, when coupled with TiO$_2$ or ZnO. XPS further confirmed the formation of Ti-O-C and Ti-C bridge bonds between TiO$_2$ and GO. TiO$_2$-GO existed as dispersed particles having crystal morphology. ZnO-GO showed slight amorphous nature. PS-TiO$_2$-GO and PS-ZnO-GO composites were mechanically stronger and thermally more stable compared to PS-TiO$_2$ and PS-ZnO. TiO$_2$-GO and ZnO-GO composites exhibited enhanced photocatalytic efficiency compared to TiO$_2$ and ZnO respectively for the UV degradation of PS. It was also observed that TiO$_2$-GO was more efficient compared to ZnO-GO for PS degradation.

5.1. Introduction

Studies worldwide have shown that the photocatalytic property of inorganic metal oxide semiconductors has appreciably enhanced in the presence of carbon based materials like carbon nano tube[1,2], fullerene[3,4] and graphene[5,6]. The photocatalytic activities of TiO_2 and ZnO coupled with such carbon allotropes have been extensively investigated with amazing results. Out of the carbon structures, graphene has an advantage of 2D planar structure with higher surface area for better interaction with other materials and can be prepared easily in the laboratory from graphite. Graphene has some marked unique properties including enhanced electrical[7], mechanical[8], thermal[9] and optical properties[10]. Better chemical stability is also observed in this transparent and flexible material[11]. Composites of graphene find application in electronics[7], composite materials[12,13], solar cells[14], ultra capacitors[15], medicine[16,17] molecular sensors[18] and so on.

Graphene oxide (GO) could be considered as a derivative of graphene with oxygen atoms bonded covalently to some of its carbon atoms leading to hydroxyl or epoxy bonds[19–23]. Carboxylic acid functional groups may also be attached to the periphery of hexagonal two dimensional planes of GO[24]. Even though GO shows slight variations in some of the properties compared to graphene, like conductivity[25], GO resembles graphene in many other aspects. Graphene could be replaced by GO where improved hydrophilicity is demanded. The functional groups >C=O, -COOH and epoxy, covalently bonded to some of the carbon atoms in GO provides better interaction with polar solvents especially water. GO is hence highly dispersible in water[26,27]. Graphene, on the other hand, is not dispersible in aqueous media. The existence of strong molecular interaction between GO and metal oxides in composites have been reported[28]. The interaction between GO and metal oxides are possible in a number of ways including the formation of hydrogen bonds, M-C[29] and M-O-C[30–33] bonds where M refers to the metal atoms in metal oxides, C for carbon and O for oxygen. These bonds act as bridges, facilitating easy charge transport between the metal oxides and GO. The properties of GO and metal oxides are entirely altered into new properties related to the composite. One of the most important properties of metal oxide-GO composite materials is related to its bandgap energy[34]. The bandgap energy of metal oxide–GO composites is lower compared to that of metal oxides. The

relevance of such bandgap shift comes into picture when the metal oxides like TiO_2 and ZnO with high bandgap energies that absorb only in the UV region, are shifted into modified materials with lower bandgap energies upon surface modification with GO. The lowering of bandgap energy allows the material to absorb in the UV as well as in the visible region extending its application to broad areas.

Decreased rate of recombination of photogenerated electrons and holes of metal oxides are observed in metal oxide-GO composites. The electrons in the conduction band of metal oxides are transferred into the carbon atoms of GO. These electrons are resonance stabilized in GO and their recombination with the holes in metal oxides are hence minimized[35]. Interfacial charge transfer of TiO_2-GO and ZnO-GO has been reported with heterojunctions of enhanced photocatalytic activity[36,37].

Photodegradation of PS in the presence of TiO_2 as well as ZnO coupled with Graphene oxide (GO) is discussed in this chapter. GO has been selected instead of graphene for surface modification of TiO_2 and ZnO keeping the following aspects in mind: (i) GO bears similar properties as graphene. (ii) GO could stabilize ZnO or TiO_2 much easier than graphene by various interactions. (iii) The oxygen containing functional groups present in GO can interact with electrons from ZnO or TiO_2 forming a bridge between them facilitating easier charge transfer. (iv) The functional groups present in GO can produce radicals when exposed to UV radiation for the initiation of photochemical reaction. (v) Preparation of GO is easier compared to graphene (vi) GO can be dispersed much easily in a wide variety of polar solvents compared to graphene so that TiO_2-GO or ZnO-GO composite preparation becomes easier.

Out of numerous methods of preparation of GO, the most widely adopted one is the oxidation of graphite developed by Hummers and Offeman in 1958[38]. Modified Hummers methods are commonly used nowadays. In this strategy, oxidizing agents are penetrated between the layers of graphite resulting in the separation of GO layers and finally the oxidation reaction is terminated with the aid of H_2O_2 and water[39,40]. The mechanism of GO formation through three stages involves the formation of H_2SO_4-graphite intercalation compound followed by its oxidation and reaction with water as reported by A.M. Dimiev and J.M. Tour in 2014[41]. The advantages of GO

preparation by Hummers or modified Hummers method are the elimination of evolution of explosive gases and decrease of reaction time[42].

Section I

Synthesis and characterisation of TiO₂-GO and ZnO-GO composites

5.2. Experimental

5.2.1. Synthesis of Graphene oxide (GO)

GO was prepared from graphite (150 mesh) through modified Hummers method. Typically 23 ml of sulphuric acid was cooled to 0°C in a flask to which 1g of graphite and 0.5 g $NaNO_3$ were added slowly with stirring over an ice bath. Vigorous stirring was continued for 40 minutes. 3g $KMnO_4$ was then added to this mixture while stirring was in progress, very slowly and in a controlled way, maintaining the temperature of the system below 20°C. A dark green viscous solution was obtained. Vigorous stirring was continued for another 12 hours at room temperature. To the viscous paste like reaction mixture, 40 ml distilled water was added. The dark brown mixture hence obtained was subjected to stir for another 24 hours followed by the slow addition of 10 ml 30% H_2O_2. The mixture turned yellowish brown in colour. Stirring was continued for another 6 hours. The solution hence obtained was washed 20 times thoroughly using 1M HCl followed by distilled water using a laboratory centrifuge until the pH of the solution reached 6. pH 7 could not be reached by washing the solid GO residue obtained using water practically. So the solid GO hence obtained was dried at 80°C for 12 hours in a hot air oven and finally a brownish black thin film of GO was obtained[28,43].

5.2.2. Synthesis of TiO₂-GO composite

TiO₂-GO composites were prepared by ultrasonication assisted hydrothermal process. TiO₂-GO composites with 1, 3, 10 and 30 weight percentages of GO namely TiO₂-1% GO, TiO₂-3% GO, TiO₂-10% GO and TiO₂-30% GO were prepared respectively. In order to prepare TiO₂-1% GO, 8 mg of GO was dispersed in 80 ml

water and 40 ml ethanol by vigorous sonication using an ultrasonic probe sonicator (750 W) for two hours in a flask. 800 mg of nano TiO_2 was added to the flask and the sonication was continued for another two hours. The temperature of the flask was maintained using an ice bath in order to prevent evaporation of solvents due to excess heating. The contents of the flask were transferred into a Teflon lined hydrothermal autoclave which was kept in a hot air oven at a temperature 130°C for 6 hours. The bluish grey solid residue hence obtained was filtered out from the solution and dried at 70°C for 12 hours in a hot air oven. TiO_2-3% GO, TiO_2-10% GO and TiO_2-30% GO composites were prepared by the same route varying the weight percentages of GO taken[44–46].

5.2.3. Synthesis of ZnO-GO

ZnO-GO composites were also prepared by ultrasonication assisted hydrothermal process. ZnO-GO composites with 3, 10 and 30 weight percentages of GO namely ZnO-3% GO, ZnO-10% GO and ZnO-30% GO were prepared. For the preparation of ZnO-3% GO, 30 mg of GO was dispersed in 40 ml water and sonicated for 2 hours. 1.55 g of zinc nitrate hexahydrate ($Zn(NO_3)_2.6H_2O$) was added to the dispersion. Liquid ammonia was added dropwise with vigorous stirring until a white precipitate of $Zn(OH)_2$ was formed. The entire mixture was then transferred into a Teflon lined hydrothermal autoclave which was kept in a hot air oven at a temperature 130°C for 6 hours. The solid residue hence obtained was filtered, washed with distilled water and dried at 70°C for 12 hours in a hot air oven. ZnO-10% GO and ZnO-30% GO were also prepared in similar way by changing the weight percentage of GO[47,48].

5.3. Results and Discussion

5.3.1. Powder XRD

Powder XRD pattern of prepared GO exhibits its characteristic intense peak at an angle $2\theta=10.7°$ corresponding to the (001) plane of GO. In addition to this, a broader peak of very low intensity was also observed at an angle $2\theta=26°$ corresponding to the unoxidized graphite and/or reduced GO present in traces (Figure 5.1.1).

XRD patterns of TiO_2-GO composites exhibited all the peaks corresponding to TiO_2 (Figure 5.1.1). The peak corresponding to GO was hampered and invisible in

TiO$_2$-GO composites. The dispersion of nano sized GO layers and their association with TiO$_2$ without any aggregation made the presence of GO undetectable through XRD. The absence of the characteristic peak corresponding to GO (2θ=10.7°) also suggests the possibility of partial reduction of GO in TiO$_2$ composites upon hydrothermal treatment (as confirmed through Raman spectroscopy and XPS analysis discussed below). Peak sharpening were also observed in TiO$_2$-GO composites compared to pristine TiO$_2$ probably due to the increase in size of the composite particles with the incorporation of GO. The inter planar distance (d) calculated using Bragg's equation showed a slight decrease for the TiO$_2$-GO composites compared to that of pristine TiO$_2$ (Table 5.1.1). Crystallite sizes calculated from Debye Scherrer's formula was greater for TiO$_2$-GO composites as compared to pristine TiO$_2$ (Table 5.1.3)[49,50].
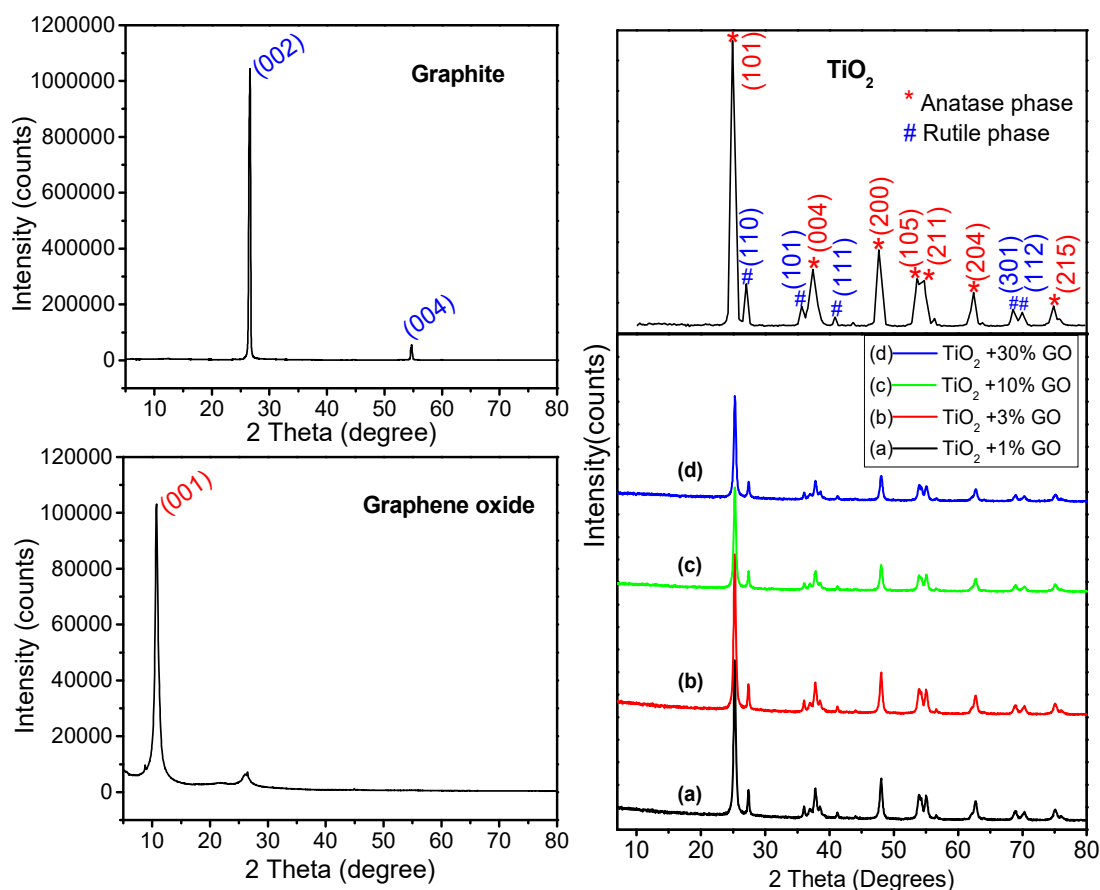

Figure 5.1.1. XRD patterns of graphite, GO, TiO$_2$ and TiO$_2$-GO composites.

XRD patterns of all the ZnO-GO composites exhibited the characteristic peaks of ZnO (Figure 5.1.2). XRD patterns of ZnO-3% GO resembled that of ZnO. For ZnO-10% GO composite new broad patterns between 2θ=20 to 28° corresponding to

reduced GO was observed. In addition to this, broad peaks at 2θ=12.8°, 33° and 59.6° corresponding to $Zn(OH)_2$ were also observed. The intensity of the peaks corresponding to reduced GO as well as $Zn(OH)_2$ increased in ZnO-30%GO composite. Inter planar distance (d) of the composites were calculated from Bragg's equation (Table 5.1.2) and crystallite sizes were calculated using Debye Scherrer's equation (Table 5.1.3). Crystallite sizes of the composites were slightly higher compared to that of pristine ZnO.
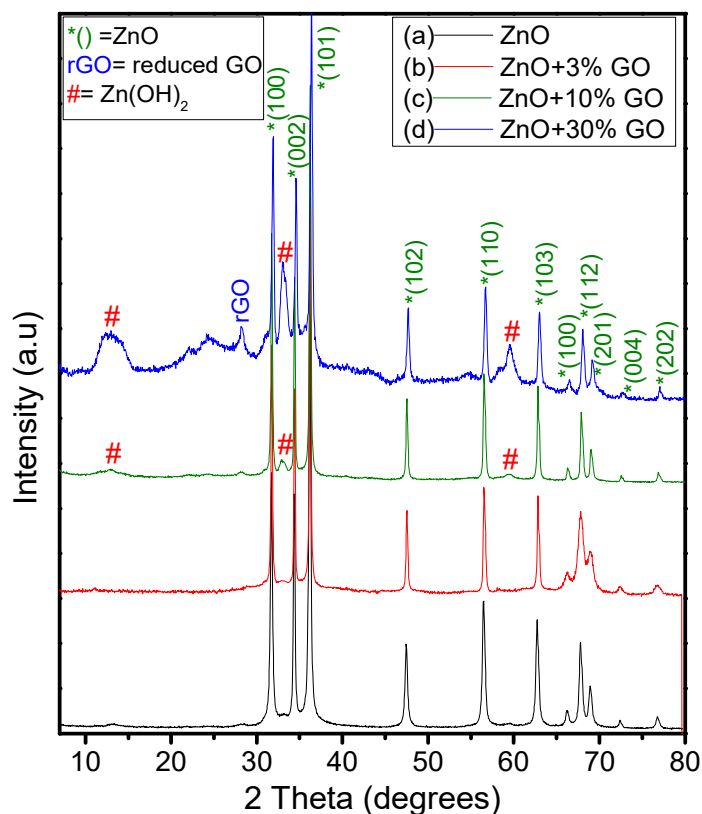

Figure 5.1.2. XRD patterns of ZnO and ZnO-GO composites.

Table 5.1.1. *Inter planar distances (d) corresponding to 2θ peaks of TiO_2 and TiO_2-GO composites*

	TiO_2		TiO_2-1%GO		TiO_2- 3% GO		TiO_2-10%GO		TiO_2-30%GO	
	2 θ°	**d (Å)**	**2 θ°**	**d (Å)**	**2 θ°**	**d (Å)**	**2 θ°**	**d (Å)**	**2 θ°**	**d (Å)**
Anatase phase	24.9	3.573	25.2	3.531	25.3	3.517	25.3	3.517	25.3	3.517
	37.4	2.403	37.8	2.378	37.8	2.378	37.8	2.378	37.8	2.378
	47.7	1.905	48.1	1.89	48.1	1.89	48.1	1.89	48.1	1.89
	53.6	1.708	53.8	1.703	53.8	1.703	53.8	1.703	53.8	1.703
	54.7	1.677	54.9	1.671	55	1.668	55	1.668	55	1.668
	62.4	1.487	62.7	1.481	62.7	1.481	62.7	1.481	62.7	1.481
	74.8	1.268	75.1	1.264	75.1	1.264	75.1	1.264	75.1	1.264

	27.1	3.288	27.4	3.252	27.4	3.252	27.4	3.252	27.4	3.252
	35.7	2.513	36	2.493	36.1	2.486	36.1	2.486	36.1	2.486
Rutile phase	40.8	2.21	41.2	2.189	41.2	2.189	41.2	2.189	41.2	2.189
	68.6	1.367	69.9	1.345	70	1.343	70	1.343	70	1.343
	70	1.343	70.3	1.338	70.3	1.338	70.3	1.338	70.3	1.338

Table 5.1.2. *Inter planar distances (d) corresponding to 2θ peaks of ZnO and TiO2-GO composites*

ZnO		ZnO-3%GO		ZnO-10% GO		ZnO-30%GO	
2 θ°	d (Ă)	2 θ°	d (Ă)	2 θ°	d (Ă)	2 θ°	d (Ă)
31.97	2.80	31.98	2.79	31.98	2.79	31.98	2.79
34.62	2.59	34.65	2.59	34.65	2.59	34.65	2.59
36.45	2.46	36.47	2.46	36.47	2.46	36.47	2.46
47.71	1.90	47.73	1.9	47.73	1.9	47.73	1.9
56.75	1.62	56.77	1.6	56.77	1.6	56.77	1.6
63.01	1.47	63.05	1.47	63.05	1.47	63.05	1.47
66.48	1.41	66.5	1.4	66.5	1.4	66.5	1.4
68.05	1.38	68.07	1.38	68.07	1.38	68.07	1.38
69.18	1.36	69.2	1.36	69.2	1.36	69.2	1.36
72.70	1.30	72.73	1.3	72.73	1.3	72.73	1.3
77.00	1.24	77.03	1.24	77.03	1.24	77.03	1.24

Table 5.1.3 *Crystallite size of TiO2-GO and ZnO-GO composites calculated using Debye- Scherrer equation.*

	Crystallite size (nm)		Crystallite size (nm)
TiO_2	17.57	ZnO	30.7
TiO_2-1%GO	20.12	ZnO - 3% GO	38.65
TiO_2- 3% GO	20.27	ZnO -10%GO	38.83
TiO_2-10%GO	20.32	ZnO -30%GO	38.99
TiO_2-30%GO	20.38		

5.3.2. FTIR Spectroscopy

FTIR spectra of GO exhibited its characteristic peaks which included >C=O (1719 cm^{-1}), >C=C< (1622 cm^{-1} and 1519 cm^{-1}), -C-O- (1065 cm^{-1} and 963 cm^{-1}), -OH stretching (3600-3000 cm^{-1}), -C-O-H bending (1377 cm^{-1}) and -C-H out of plane bending vibrations (673 cm^{-1}) (Figure 5.2). The presence of carboxylic acid and hydroxyl functional groups in GO were hence quite evident. FTIR spectra of TiO_2-GO composites exhibited characteristic vibration peaks corresponding to TiO_2 as well

as GO (Figure 5.2 A). A striking observation made from the IR spectra was that a considerable shift towards lower wavenumber in the peak positions occurred in TiO_2-GO composites when compared to uncoupled GO. With the increase in percentage incorporation of GO among the composites, peaks corresponding to >C=O and -C-O-H functional groups exhibited an observable shift. This observation suggested the existence of a strong interaction between TiO_2 and the oxygen atom of acid or alcoholic functional groups of GO. Increase in the intensities of IR absorption peaks of GO were also observed in the composites as the percentage of GO incorporation increased. Tabulated FTIR data of TiO_2-GO composites in comparison to GO is given in table 5.2.1.
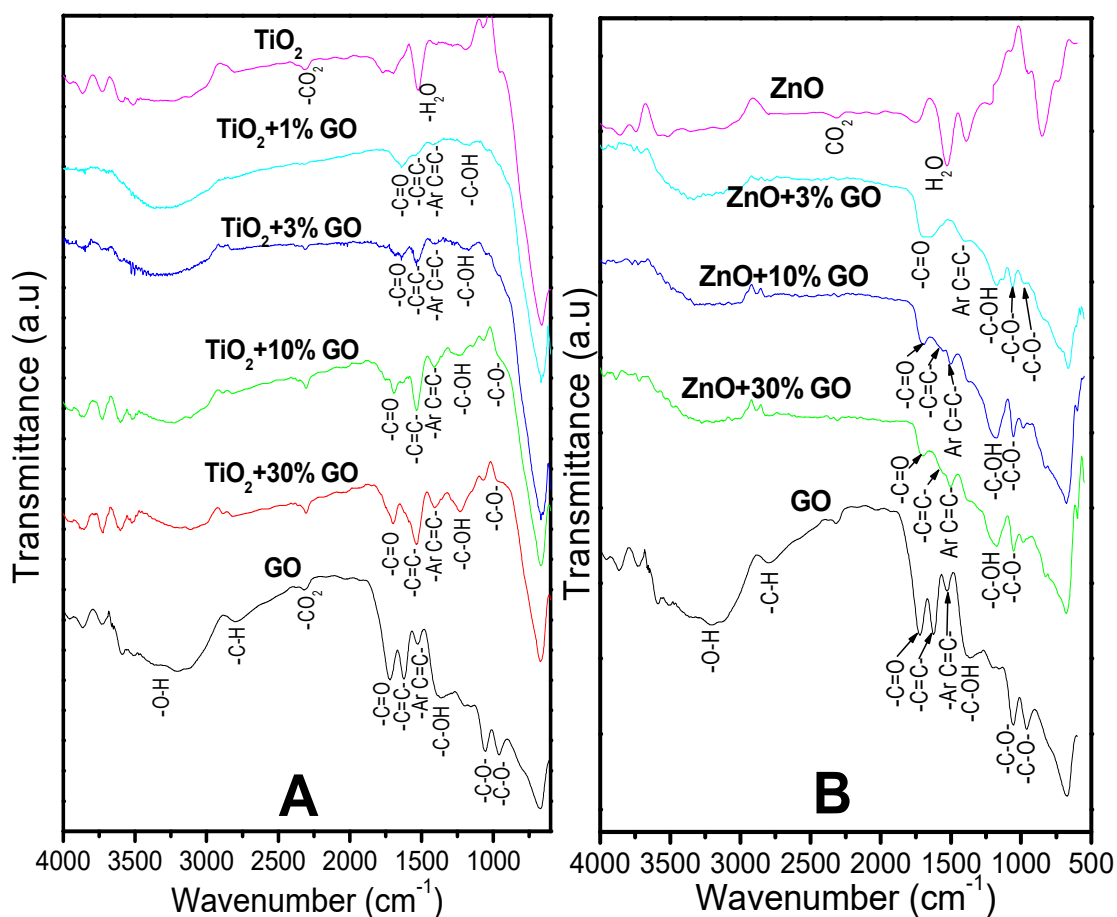
Figure 5.2*. FTIR spectra of TiO_2-GO composites (A) and ZnO-GO composites (B) in comparison with that of GO, TiO_2 and ZnO.*

Similar observations were made from FTIR spectra of ZnO-GO composites (Figure 5.2 B). The characteristic vibration bands of GO shifted towards lower wavenumber positions in ZnO-GO composites due to the interaction between ZnO

and GO. The shift in peak positions of >C=O and -C-O-H functional groups among ZnO-GO composites as the percentage of GO increased, suggested a strong interaction between ZnO and the oxygen atom of the acid or the alcoholic functional groups of GO. The tabulated FTIR data of ZnO-GO composites in comparison to GO is given in table 5.2.2.

Table 5.2.1. Highlighted peaks from FTIR spectra of GO and TiO₂-GO composites

	GO	TiO₂+30%GO	TiO₂+10%GO	TiO₂+3%GO	TiO₂+1%GO
>C=O (stretch)	1719 cm⁻¹	1699 cm⁻¹	1695 cm⁻¹	1645 cm⁻¹	1640 cm⁻¹
>C=C< (Stretch)	1622 cm⁻¹	1536 cm⁻¹	1536 cm⁻¹	1536 cm⁻¹	1536 cm⁻¹
Ar-C=C (Stretch)	1519 cm⁻¹	1412 cm⁻¹	1410 cm⁻¹	1408 cm⁻¹	1408 cm⁻¹
-C-O-H (bend)	1377 cm⁻¹	1232 cm⁻¹	1224 cm⁻¹	1176 cm⁻¹	1165 cm⁻¹
-C-O- (Stretch)	1065 cm⁻¹	Overlapped by Ti-O stretching vibrational peaks			
-C-O- (Stretch)	963 cm⁻¹	962 cm⁻¹	Overlapped by Ti-O stretching vibrational peaks.		

Table 5.2.2. Highlighted peaks from FTIR spectra of GO and ZnO-GO composites

	GO	ZnO+30%GO	ZnO+10%GO	ZnO +3%GO
>C=O (stretch)	1719 cm⁻¹	1704 cm⁻¹	1695 cm⁻¹	1690 cm⁻¹
>C=C< (Stretch)	1622 cm⁻¹	1558 cm⁻¹	1556 cm⁻¹	Overlapped by Ar-C=C band
Ar-C=C (Stretch)	1519 cm⁻¹	1505 cm⁻¹	1501 cm⁻¹	1403 cm⁻¹
-C-O-H (bend)	1377 cm⁻¹	1178 cm⁻¹	1175 cm⁻¹	1170 cm⁻¹
-C-O- (Stretch)	1065 cm⁻¹	1054 cm⁻¹.	Overlapped by Zn-O stretching vibrational peaks	
-C-O- (Stretch)	963 cm⁻¹	Overlapped by Zn-O stretching vibrational peaks.		

5.3.3. Raman Spectroscopy

GO and TiO₂-GO was analysed through Raman spectroscopy in order to study the structure and bonding within TiO₂-GO composite in detail. Raman spectra of GO presented in Figure 5.3a displays two bands at 1355 cm⁻¹ (D band) and 1587 cm⁻¹ (G band). The D band represents the disorder of sp³ carbon atom (having A₁g symmetry)

whereas G band could be attributed to the in-plane sp^2 carbon (E_{2g} symmetry) vibrational mode of graphene skeleton. Raman spectra of TiO_2-30% GO (Figure 5.3b) also shows D and G bands of graphene moiety. Bands observed at 154 cm^{-1}, 394 cm^{-1}, 511 cm^{-1} and 634 cm^{-1} could be attributed to $E_{g(1)}$, $B_{1g(1)}$, $A_{1g}+ B_{1g(2)}$ and $E_{g(2)}$ respectively of anatase phase TiO_2. A band at 2695 cm^{-1} was also observed in TiO_2-30% GO composite that attributes the characteristic 2D band of sp^2 carbon of graphene. This band was however not observed in the spectra of GO. The appearance of 2D band reveals the presence of reduced GO associated with TiO_2 in the composite. The ratio of intensities of D and G bands (I_D/I_G) calculated to be 0.93 in GO decreased to 0.62 in TiO_2-30% GO. The decrease in the I_D/I_G value shows that some of the sp^3 bonds have been converted in to sp^2 (or decrease in structural defects within sp^2 carbon) as a consequence of partial reduction of GO in TiO_2-GO composite.
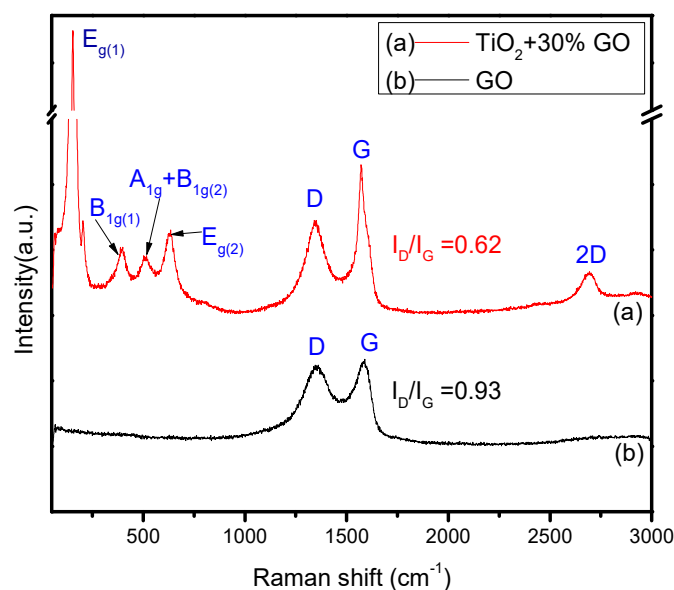
Figure 5.3*. Raman spectra of GO (a) and TiO₂-30% GO (b) composite*

5.3.4. X-ray photoelectron spectroscopy (XPS)

The interaction between TiO_2 and GO in TiO_2-GO composites was further clear from XPS analysis of GO and TiO_2-30%GO (Figure 5.4). XPS revealed the fact that partial reduction of GO took place in TiO_2-30%GO composites with the formation of Ti-C and Ti-O-C bonds, between TiO_2 and GO. Bands corresponding to C 1s and O 1s were observed in the XPS of GO and the bands corresponding to Ti 2p, C 1s and O 1s were observed in the XPS of TiO_2-30%GO (Figure 5.4 A).
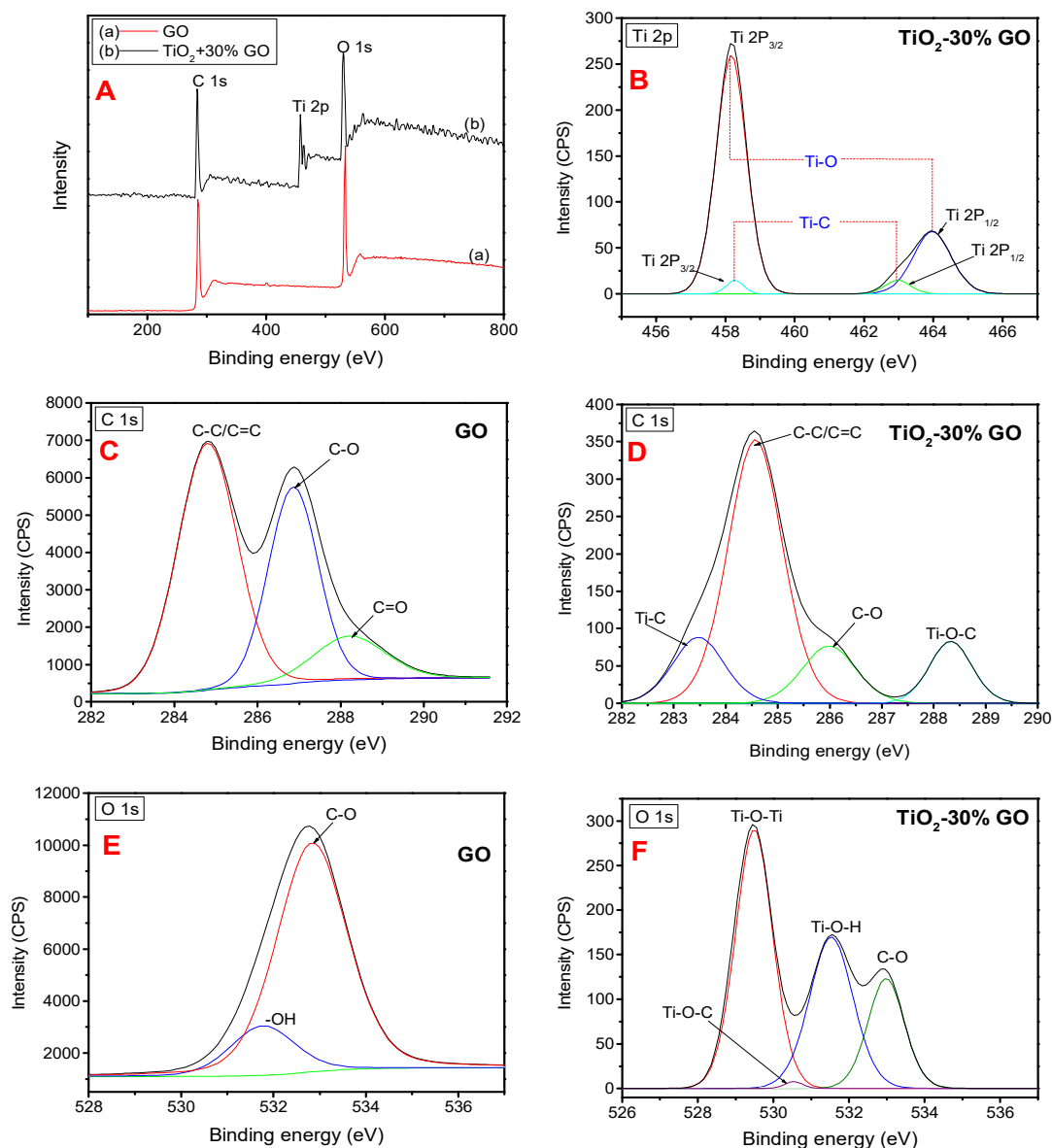
Figure 5.4. *XPS of GO and TiO₂-30%GO (A). Deconvoluted XPS of Ti 2p, C 1s and O 1s regions of GO and TiO₂-30% GO composite (B to F).*

The deconvoluted spectra of C 1s region of GO exhibited three peaks corresponding to the binding energies 284.7 eV, 286.8 eV and 288.1 eV that could be assigned to C-C/C=C, C-O and C=O bonds respectively (Figure 5.4 B). C 1s region of TiO₂-30% GO composite (Figure 5.4 E) showed that the intensity of C-O binding energy peak decreased considerably compared to the C-O peak in C 1s region of GO. This is a clear evidence of partial reduction of GO. The C=O bond observed in GO was shifted to higher binding energy (288.5 eV) in TiO₂-30% GO composite due to the formation of Ti-O-C bond between TiO₂ and GO. A new peak centered at 283.4 eV represents Ti-C bond formed between TiO₂ and GO. The O 1s region of GO showed a peak

centered at 532.9 eV representing -OH bond and a less intense peak at 531.8 representing C-O bond (Figure 5.4 C). O 1s region of TiO$_2$-30% GO composite displayed peaks centered at 529.4 eV, 530.5 eV, 531.5 eV and 532.95 eV representing Ti-O-Ti, Ti-O-C, Ti-O-H and C-O bonds respectively (Figure 5.4 F). The deconvoluted spectra of Ti 2p region of TiO$_2$-30%GO composite gave four peaks (Figure 5.4 D). The peaks at 458.1 eV (2p$_{3/2}$) and 463.9 eV (2p$_{1/2}$) originated from the Ti-O bond existing in the composite. Low intense peaks centered at 458.3 eV (2p$_{3/2}$) and 462.9 eV (2p$_{1/2}$) on the other hand originated from Ti-C bond in the composite. The existence of strong interaction between TiO$_2$ and GO that could facilitate easy transport of photo generated charges between the composites was evident through XPS.

5.3.5. UV-visible Diffused reflectance spectroscopy (UV-DRS)
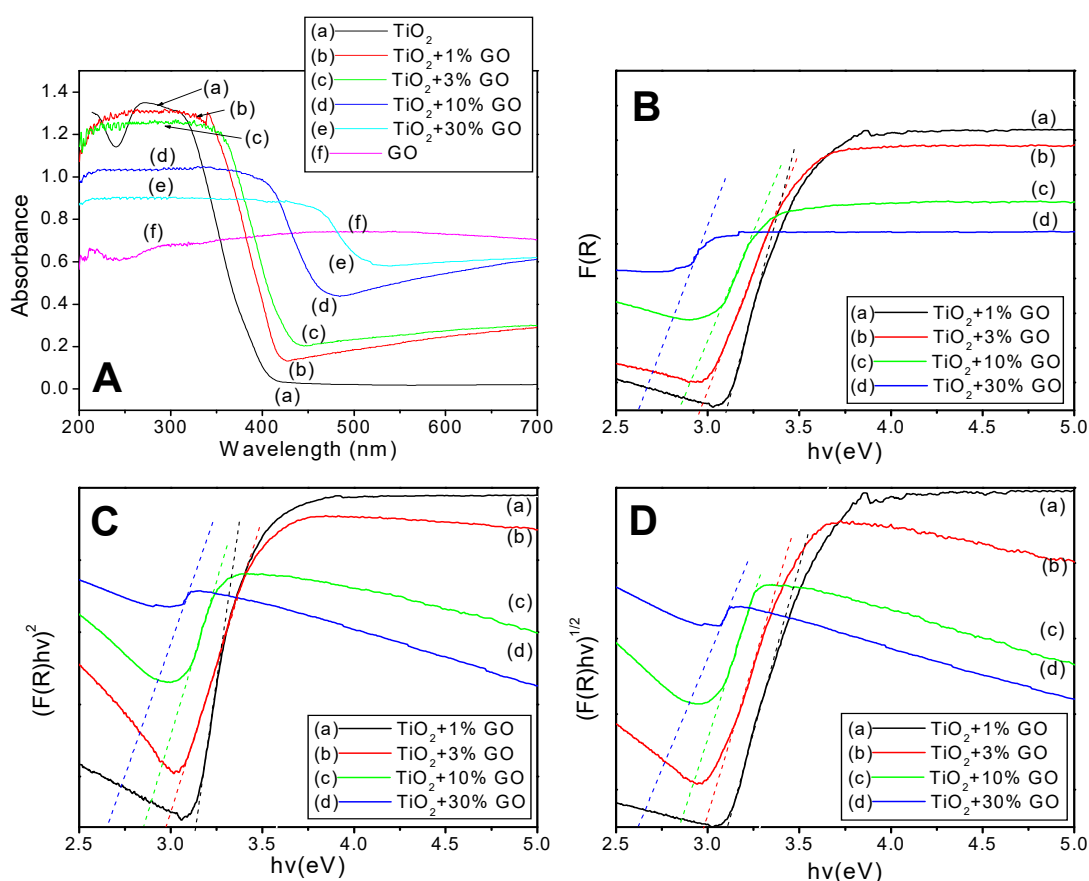
Figure 5.5.1. *UV-DRS of TiO$_2$, GO & TiO$_2$-GO composites (A). Optical bandgap energy (Eg) determination of TiO$_2$ and TiO$_2$-GO composites (B,C & D)*

UV-visible spectra obtained from UV-DRS technique showed a decrease in the characteristic absorption band in the UV region of nano TiO$_2$ upon GO incorporation.

A decrease in the UV absorption bands contradicted by the increase in the visible region absorption bands were observed as a consequence of increasing weight percentage of GO in TiO$_2$-GO composites (Figure 5.5.1 A). The ability of TiO$_2$-GO composites by which they can absorb in the UV as well as visible region is evident here. The visually observed bluish grey colouration of the TiO$_2$-GO composites could be seen due to the absorption in the visible region. The origin of the bluish colour may be due to the reduction of some of the Ti^{4+} ions into Ti^{3+} ions during the process of GO incorporation. Interaction of TiO$_2$ with the π bonds of reduced graphene oxide might have resulted in this reduction[51]. Determination of optical bandgap energies (E$_g$) from the plots of F(R) v/s hυ (irrespective of transitions), (F(R) hυ)^2 v/s hυ (direct E$_g$) and (F(R) hυ)$^{1/2}$ v/s hυ (indirect E$_g$) was done (Figure 5.5.1 B,C &D). The E$_g$ of the TiO$_2$-GO composites were lower than that of TiO$_2$. The E$_g$ of the composites decreased as the percentage of GO increased. The values of E$_g$ of the composites are given in table 5.3.
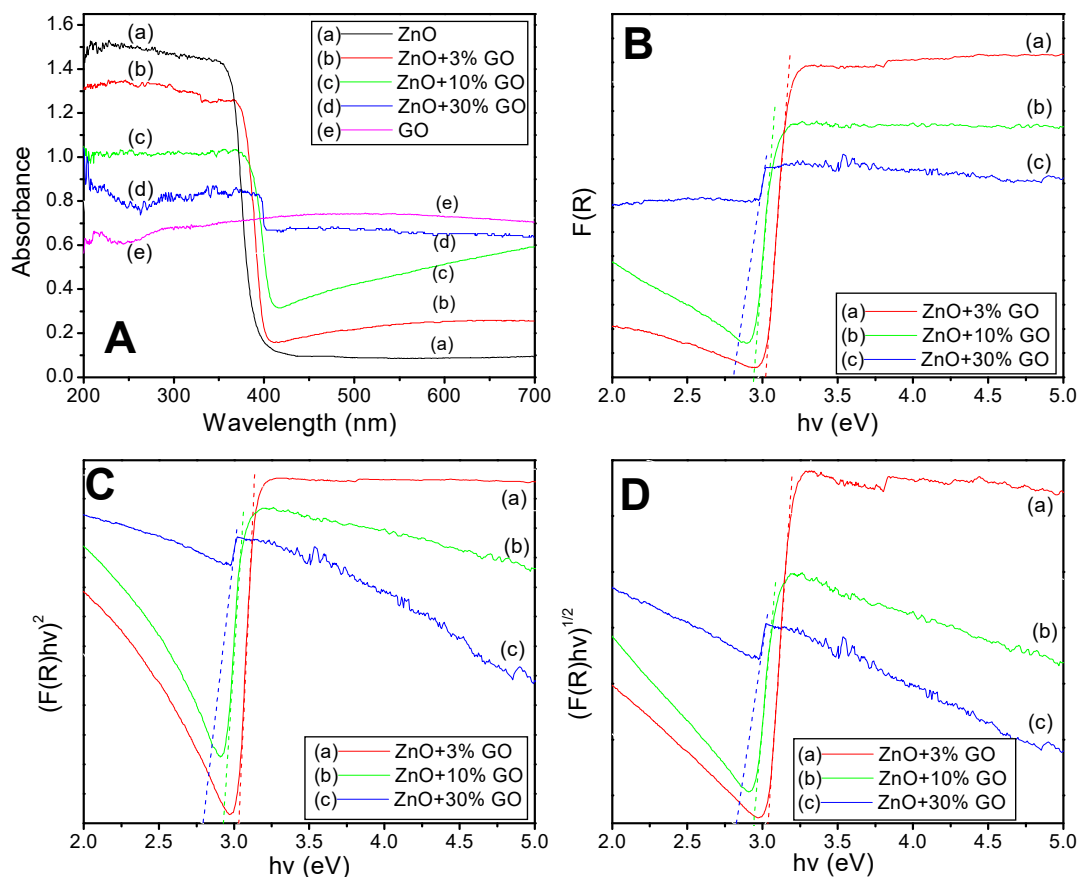
Figure 5.5.2. *UV-DRS of ZnO, GO and ZnO-GO composites (A). Optical bandgap energy (Eg) determination of ZnO and ZnO-GO composites (B, C & D)*

The UV-DRS of ZnO-GO composites followed the same trend as observed in the case of TiO_2-GO (Figure 5.5.2). The characteristic absorption bands in UV region of the spectra decreased as the percentage of GO increased. The absorption bands in visible region of the spectra on the other hand increased as the percentage of GO increased. Coupling of GO with ZnO, modified their light absorption property extending from UV region to visible region. The values of E_g of the composites (ie., E_g irrespective of transitions, direct E_g and indirect E_g) were lower than that of ZnO. A decrease in E_g among the ZnO-GO composites was noticed as the percentage of GO increased. Figure 5.5.2 B, C & D represent the plots $F(R)$ v/s $h\upsilon$, $(F(R) h\upsilon)^2$ v/s $h\upsilon$ and $(F(R) h\upsilon)^{1/2}$ v/s $h\upsilon$ of ZnO-GO composites. The values of E_g are given in table 5.3.

Table 5.3. Values of optical bandgap energies of TiO_2- GO and ZnO-GO.

Method	Band gap Energy in eV				
	TiO_2	TiO_2 +1%GO	TiO_2 +3%GO	TiO_2 +10%GO	TiO_2 +30%GO
$F(R)$ vs $h\upsilon$	3.16	3.10	2.96	2.84	2.62
$(F(R)h\upsilon)^2$ vs $h\upsilon$	3.22	3.13	2.97	2.85	2.65
$(F(R)h\upsilon)^{1/2}$ vs $h\upsilon$	3.18	3.11	2.98	2.84	2.62
Method	Band gap Energy in eV				
	ZnO	ZnO +3%GO	ZnO +10%GO	ZnO +30%GO	
$F(R)$ vs $h\upsilon$	3.2	3.02	2.93	2.80	
$(F(R)h\upsilon)^2$ vs $h\upsilon$	3.25	3.03	2.94	2.80	
$(F(R)h\upsilon)^{1/2}$ vs $h\upsilon$	3.27	3.03	2.94	2.80	

5.3.6. SEM-EDX, HRTEM and SAED

SEM image revealed that the prepared TiO_2-GO composites existed as nanoparticles (Figure 5.6.1 A). Atomic percentages of titanium, oxygen and carbon were 15.92, 50.93 and 33.15 respectively as detected through EDX technique for TiO_2-3% GO composite (Figure 5.6.1 B). The Kα1, Kβ1 and Lα1 peaks of titanium were observed at 4.5, 4.93 and 0.45 keV respectively. Kα1 peak of oxygen was seen at 0.53 keV and that of carbon at 0.277 keV
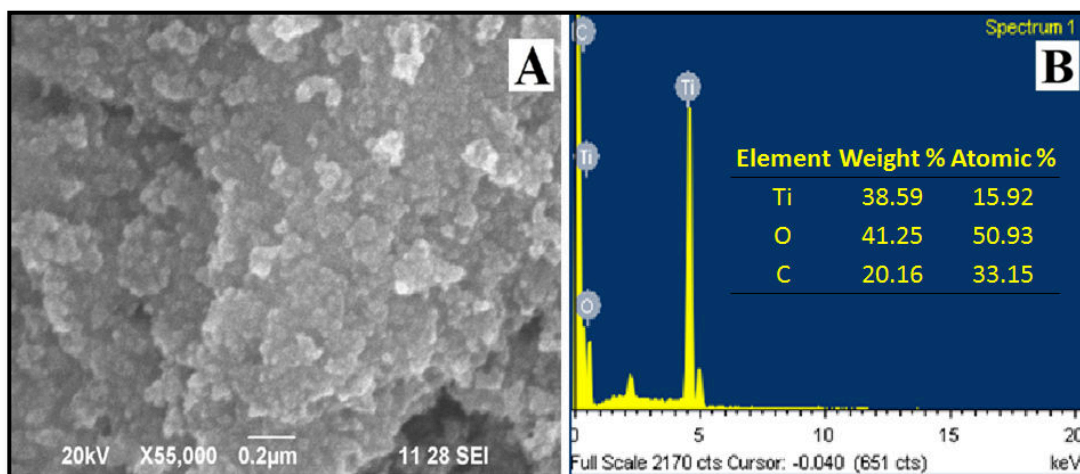
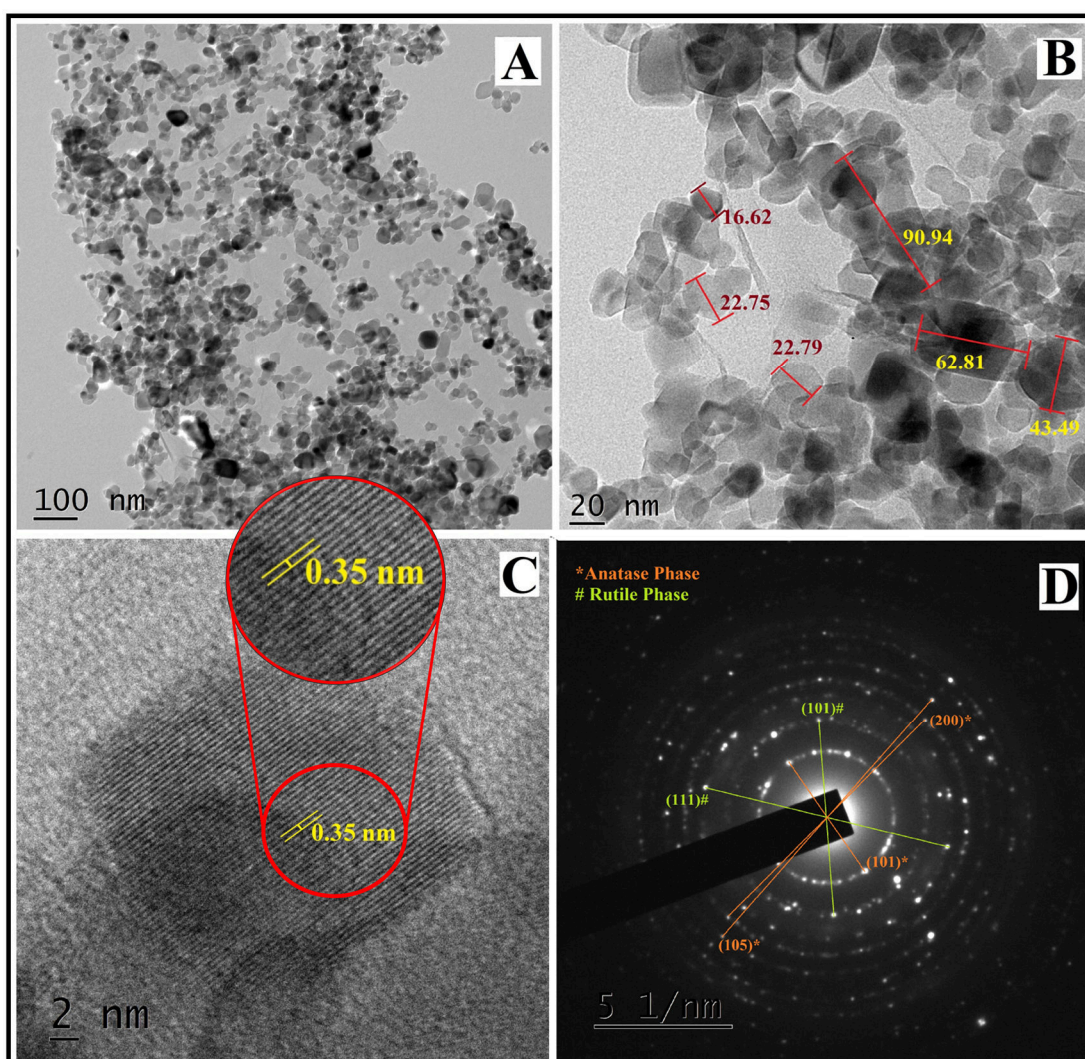*Figure 5.6.1. SEM image (A) and EDX (B) of TiO₂-30% GO composite.*

Figure 5.6.2. HRTEM image (A, B & C), SAED pattern (D) of TiO₂-3% GO

HRTEM image revealed that TiO₂-GO composite existed as separated particles. GO sheet seemed to have broken down into thin sheets of nano dimensions associated

with TiO$_2$ (Figure 5.6.2 A & B). Ultrasonication followed by hydrothermal process might have caused the sheets to break up into such nano dimensions. Lattice fringes with a spacing of 0.35 nm assigned to TiO$_2$ anatase (101) planes could be visualised through HRTEM image (Figure 5.6.2 C). Selected area electron diffraction (SAED) pattern revealed the crystalline nature of the composite with distinguished spots (Figure 5.6.2 D). Points corresponding to (101), (200) and (105) planes of anatase phase and (101), (111) planes of rutile phase TiO$_2$ were spotted from SAED patterns. The results were in well agreement with powdere XRD patterns. Average particle size was determined to be ≈ 44 nm from the HRTEM image using *image j* software.
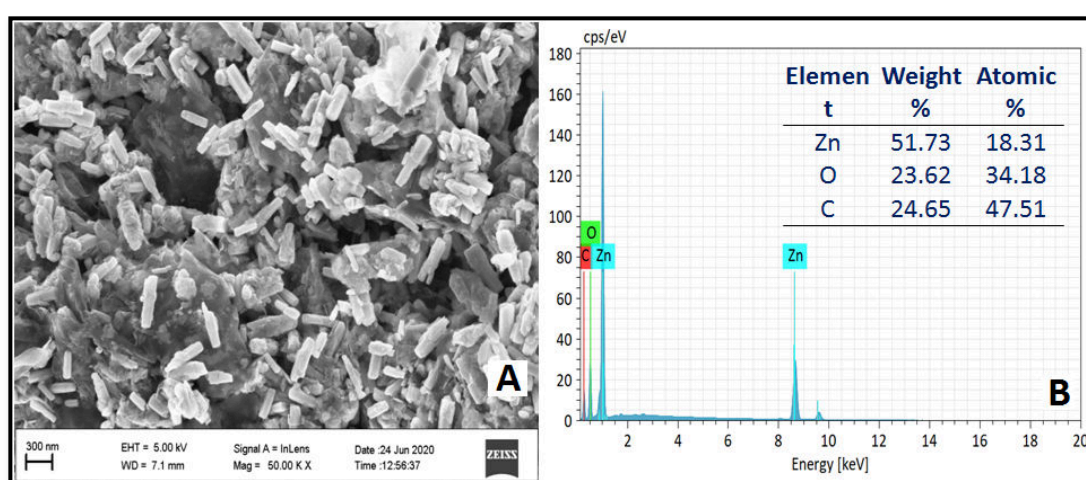
Figure 5.6.3. *FESEM image (A) and EDX (B) of ZnO-30% GO composite.*

The FESEM image of ZnO-30% GO composite showed that ZnO existed as hexagonal rods associated with GO layers (Figure 5.6.3 A). The length of the rods ranges from 90 nm to 700 nm. ZnO crystals however were bonded together by GO sheets. EDX peaks (Figure 5.6.3 B) corresponding to zinc were observed at 1.02 (Lα1, Lβ1 and Lβ3 overlap), 8.62 (overlap of Kα1 and Kα2 overlap) and 9.58 (Kβ1 and Kβ2 overlap) keV. Peak corresponding to oxygen was observed at 0.53 (Kα1) keV and that of carbon was observed at 0.277 (Kα1) keV respectively.

HRTEM of ZnO-30% GO revealed that the composites were more aggregated as compared to TiO$_2$-GO (Figure 5.6.4 A and B). The existence of ZnO particles as rods of non-uniform dimensions, observed in FESEM image were further supported by HRTEM of ZnO-30% GO composite. The GO layers existed as microsized sheets holding ZnO rods together. Some GO layers were wound around ZnO rods. The

length of the ZnO rods ranges from around 90 nm to 700 nm as observed through FESEM. Lattice fringes with a spacing of 0.28 nm assigned to (100) plane of ZnO could also be observed in the HRTEM image (Figure 5.6.4 C). SAED pattern of ZnO-30% GO composite revealed its predominant amorphous nature with halo rings (faded edges) (Figure 5.6.4 D). The spots corresponding to the plane of reduced GO (rGO), (102) and (110) planes of ZnO were however distinguished from SAED pattern of the composite.
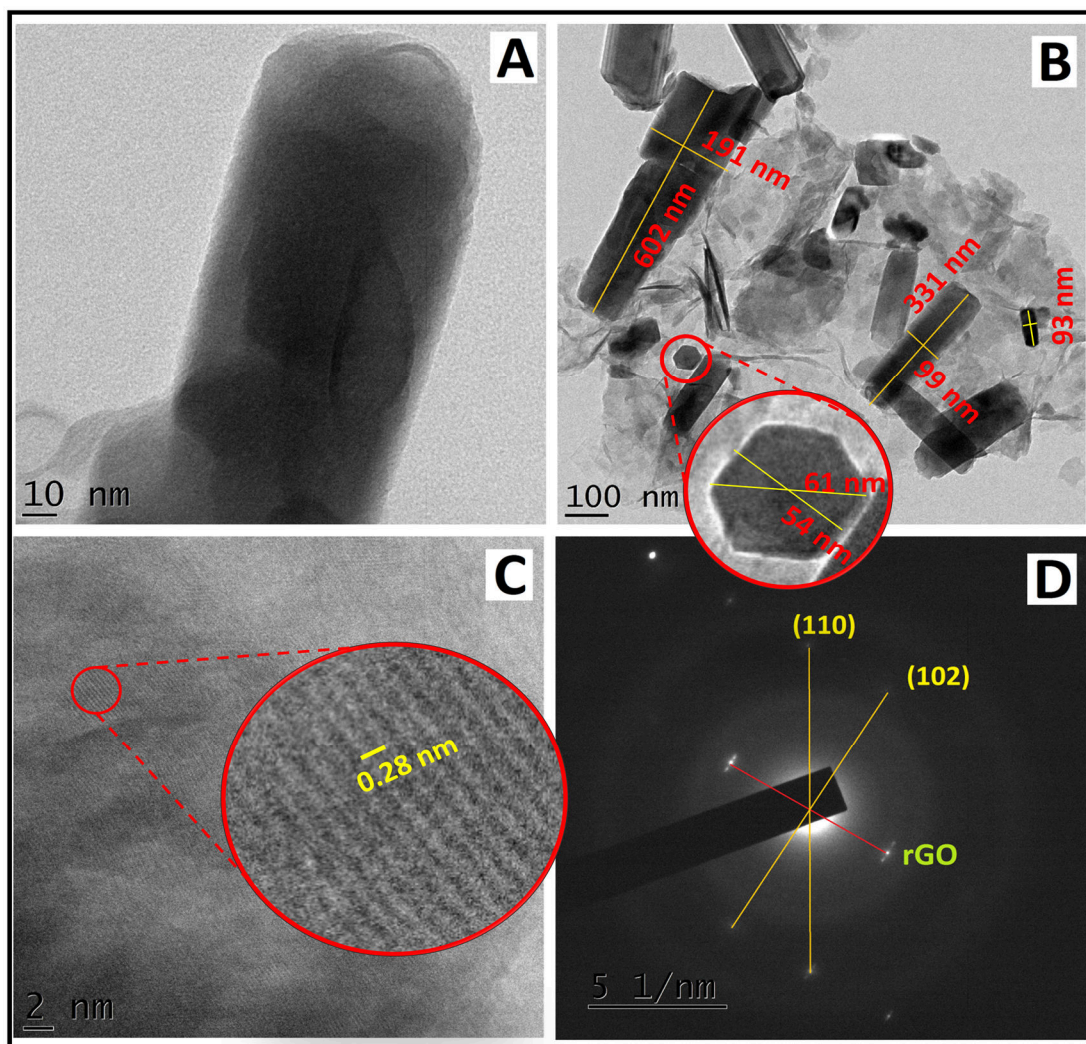

Figure 5.6.4. *HRTEM image (A,B & C), SAED pattern (D) of ZnO-30% GO*

5.3.7. Interactions of TiO$_2$/ZnO with GO in the composites

The existence of broad bands of -OH could be seen on the FTIR spectra of TiO$_2$ and ZnO as discussed in chapter 3. These broad bands of -OH vibrations arise from the OH$^-$ ions adsorbed by the surface of TiO$_2$/ZnO from the atmosphere. These -OH

groups can interact with the oxygen atoms on the >C=O or -COOH groups of GO to form hydrogen bonds as represented schematically in Figure 5.7[31]. The possibility of such hydrogen bond linkages between TiO_2/ZnO and GO cannot be ruled out as broad bands between 3500 cm^{-1} and 3000 cm^{-1} were present in FTIR spectra of TiO_2-GO as well as ZnO-GO composites.
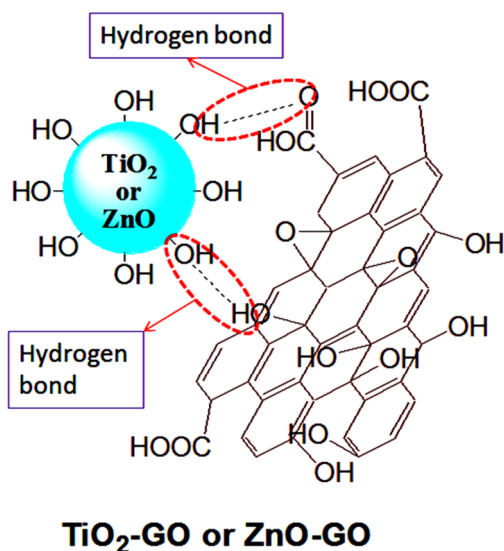

Figure 5.7. *Interaction between TiO₂-GO or ZnO-GO through hydrogen bond formation*

A considerable shift in the >C=O and >C=C< stretching bands of GO towards lower wavenumber along with the decrease in their intensities were observed in the FTIR spectra of TiO_2-GO and ZnO-GO compared to that of uncoupled GO (Figure 5.2). As the percentage of TiO_2/ZnO increased in the composites, the shift in the stretching bands increased along with the decrease in the peak intensities upto a level such that the presence of >C=C< was almost too difficult to be noticed. For the TiO_2-1% GO and ZnO-3% GO (where the percentage of TiO_2/ZnO was comparatively highest) the stretching bands of >C=O and >C=C< which were supposed to appear at the adjacent positions (1719cm^{-1} and 1622cm^{-1}) were shifted and merged almost into a single band. This shift may be explained due to the formation of Ti-O-C/Zn-O-C bond[32]. The existence of Ti-O-C bond in TiO_2-30%GO was confirmed through XPS discussed above. The condensation of -OH groups associated with TiO_2/ZnO and the functional groups present in GO leads to the formation of Ti-O-C/Zn-O-C bonds[26,52,53]. The bands corresponding to Ti-O-C bond supposed to appear at around 800-850 cm^{-1} for TiO_2-GO composites were however not clear due to the overlap of Ti-O-Ti stretching band. A peak at around 833 cm^{-1} was observed for ZnO-GO

composites which may be attributed to Zn-O-C stretching[34]. XPS analysis also showed the existence of Ti-C bond between TiO_2 and GO.

Ti-O-C/Zn-O-C and Ti-C bonds may shift the valence band of TiO_2/ZnO GO to lower level, thereby reducing the bandgap[54]. The lowering of bandgap energy (E_g) in TiO_2-GO and ZnO-GO composites was evident based on the above results.

In addition to the Ti-O-C/Zn-O-C bonds or hydrogen bond formation, the interfacial electron transfer between the heterojunctions (TiO_2-GO & ZnO-GO) is also favoured[36,37]. GO plays the role of electron acceptor which accepts electrons into its Fermi levels from the conduction band of TiO_2[35].

Section II

Photodegradation of polystyrene using TiO_2-GO and ZnO-GO composites as photocatalysts

The role of TiO_2-GO as well as ZnO-GO composites as photocatalysts in the photodegradation of PS under UV irradiation was studied. PS-TiO_2-GO and PS-ZnO-GO composites were prepared by solvent casting as discussed in chapter 2. The specimens for electrical and mechanical studies were also prepared. Photodegradation studies of the specimens were carried out. The results obtained through various monitoring techniques adopted for photodegradation studies are interpreted and discussed below.

5.4. Results and Discussion

5.4.1. Gel permeation chromatography (GPC)

The number average ($\overline{M}_n$) and weight average ($\overline{M}_w$) molecular weight of PS-TiO_2-GO (Figure 5.8.1) as well as PS-ZnO-GO (Figure 5.8.2) composites decreased as the time of UV irradiation increased. The decrease in the average molecular weight was predominant in PS-TiO_2-GO composites compared to that of PS-ZnO-GO. It was also observed that PS-TiO_2-GO and PS-ZnO-GO composites underwent a better decrease in the average molecular weights compared to that of PS-TiO_2 and PS-ZnO

composites. The maximum decrease in the average molecular weights among the PS-TiO$_2$-GO composites upon UV irradiation was observed in PS-(TiO$_2$-30% GO). The decrease in the average molecular weight in the case of PS-ZnO-GO on the other hand was observed in PS-(ZnO-10% GO). The decrease in $\overline{M}_w$ and $\overline{M}_n$ for PS-(ZnO-30% GO) was not as pronounced as that of PS-(ZnO-10% GO) composite.
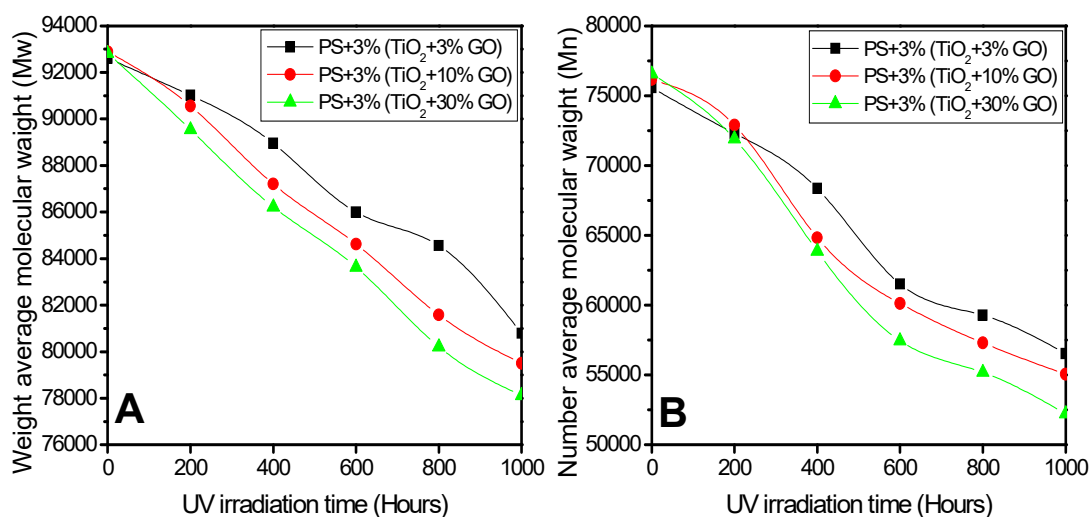

Figure 5.8.1. A) *Weight average ($\overline{M}_w$) and **B)** number average ($\overline{M}_n$) molecular weights of PS-TiO$_2$-GO composites under different UV irradiation time*
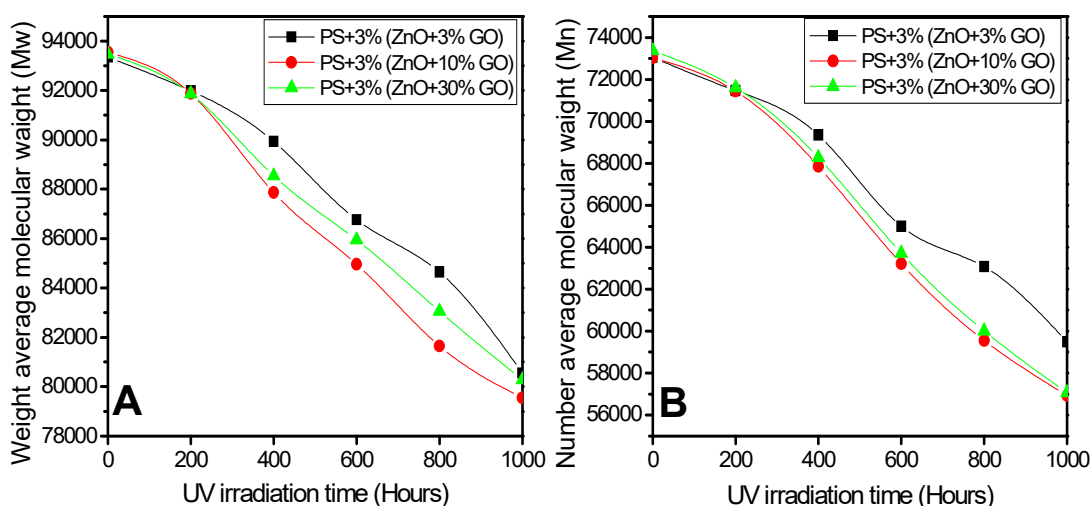
Figure 5.8.2. A) *Weight average ($\overline{M}_w$) and **B)** number average ($\overline{M}_n$) molecular weights of PS-ZnO-GO composites under different UV irradiation time*

The number of chain scissions per molecule (S) and the number of scission events per gram (N$_t$) of PS-TiO$_2$-GO (Figure 5.8.3) and PS-ZnO-GO (Figure 5.8.4) composites increased with respect to UV irradiation time. Maximum increase in the chain scissions on UV irradiation was observed for PS-(TiO$_2$-30% GO) among the

PS-TiO$_2$-GO composites. Among PS-TiO$_2$-GO composites, PS-(ZnO-10% GO) underwent maximum chain scission. The increased S and N_t of PS-TiO$_2$-GO composites were better, compared to that of PS-ZnO-GO composites.
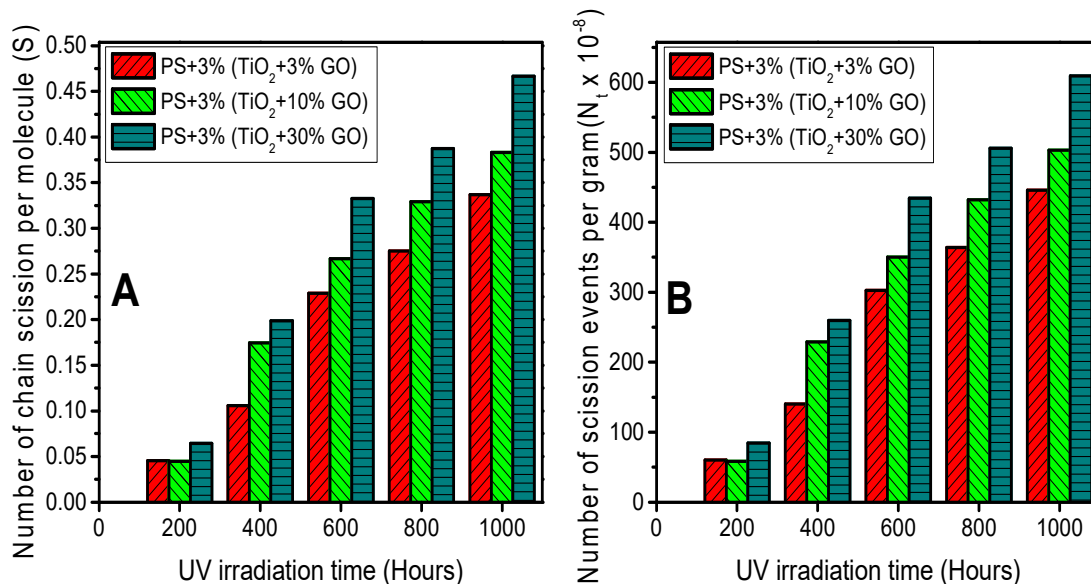

Figure 5.8.3. (A) *Number of chain scissions per molecule (S) and* ***(B)*** *number of scission events per gram (N$_t$) of PS-TiO$_2$-GO composites under different UV irradiation time intervals*
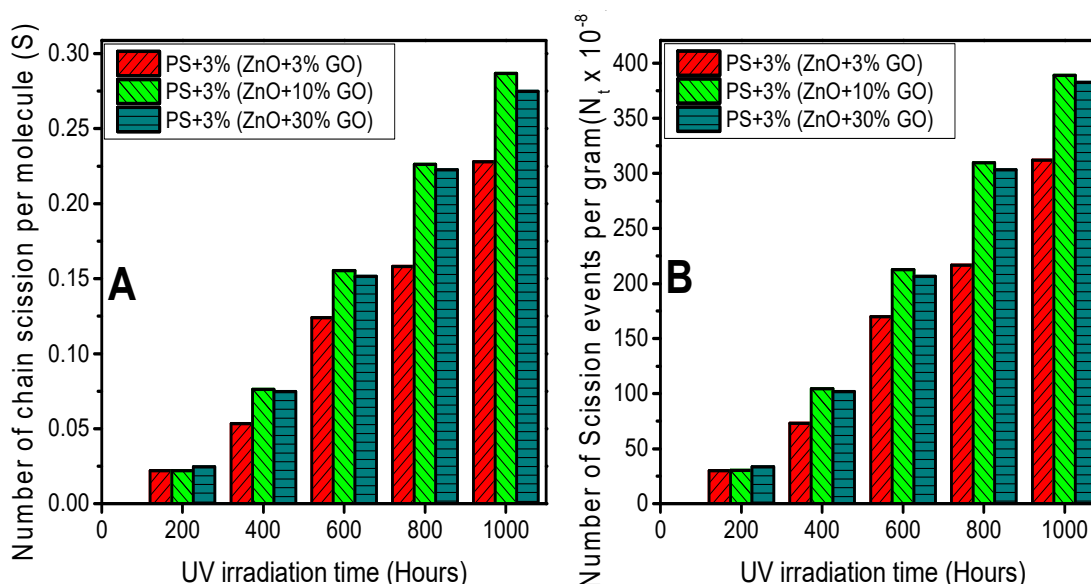

Figure 5.8.4. (A) *Number of chain scissions per molecule (S) and* ***(B)*** *number of scission events per gram (N$_t$) of PS-ZnO-GO composites under different UV irradiation time intervals*

The increase in the polydispersity index of PS-TiO$_2$-GO as well as PS-ZnO-GO composites increased as the time of UV irradiation increased (Figure 5.8.5). The increase in the randomness of chain cleavage is highlighted here.
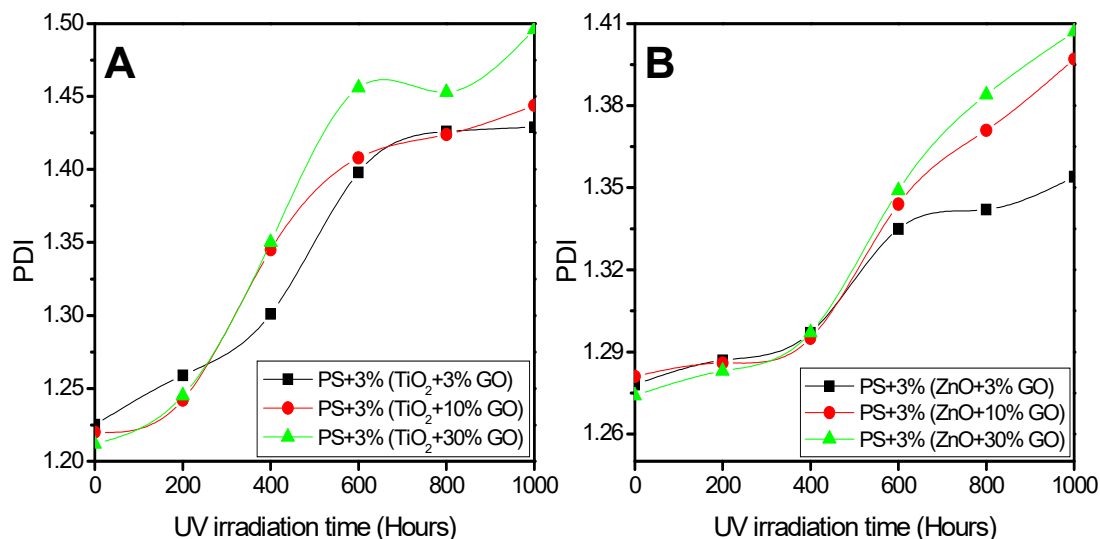

Figure 5.8.5. *Polydispersity index (PDI) of PS-TiO$_2$-GO (A) and PS-ZnO-GO (B) composites under different UV irradiation time*

5.4.2. FTIR Spectroscopy

FTIR spectra of PS-TiO$_2$-GO composites showed an increase in the intensity of stretching vibrations corresponding to >C=O (1740- 1700 cm^{-1}), -OH/ -OOH (3700-3600 cm^{-1}), >C=C< (1680-1650 cm^{-1}) etc. as the time of UV irradiation increased, suggesting photo-oxidation. We could also observe that PS-TiO$_2$-GO composites underwent better photo-oxidation compared to that of PS-TiO$_2$ composites. Enhancement in the photocatalytic efficiency of TiO$_2$ upon surface modification with GO was evident. The extent of photo-oxidation was found maximum in PS-(TiO$_2$-30% GO) composite compared to the other PS-TiO$_2$-GO composites. Photo-oxidation upon UV irradiation for PS-TiO$_2$-GO composites followed the order: PS-(TiO$_2$-30% GO) > PS-(TiO$_2$-10% GO) > PS-(TiO$_2$-3% GO) > PS-(TiO$_2$-1% GO). This trend revealed that the extent of photo-oxidation increased as the percentage of GO associated with TiO$_2$ in the composites increased. Figure 5.9.1 and 5.9.2 represents the FTIR spectra of PS-(TiO$_2$-10% GO) and PS-(TiO$_2$-30% GO) respectively.
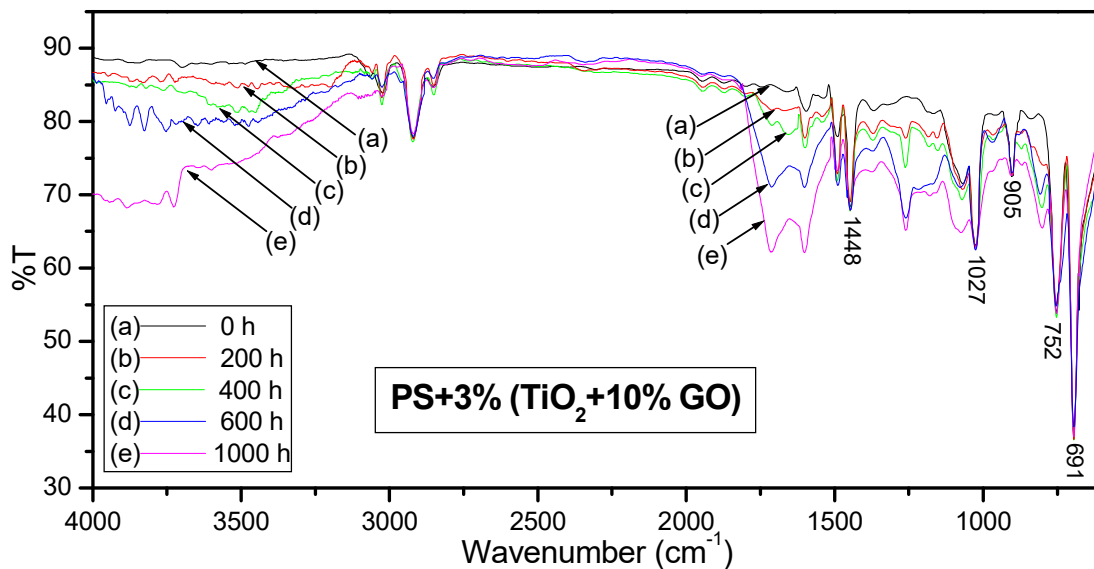
Figure 5.9.1. *FTIR spectra of PS-3%(TiO₂-10% GO) after different UV exposure time intervals ranging from 0 h to 1000 h.*
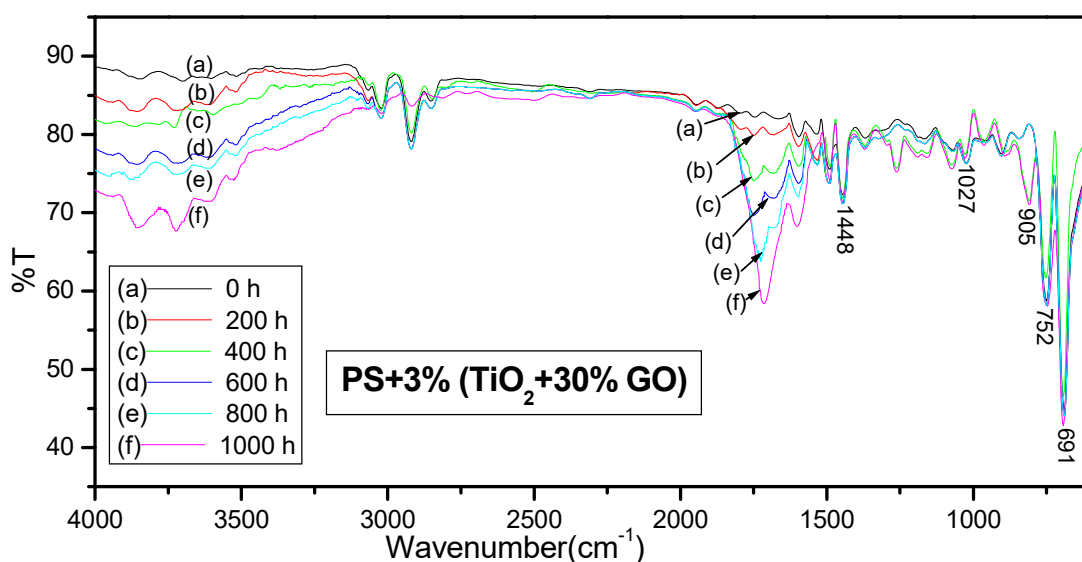

Figure 5.9.2. *FTIR spectra of PS-3%(TiO₂-30% GO) after different UV exposure time intervals ranging from 0 h to 1000 h.*

FTIR spectra of PS-ZnO-GO composites looked similar to that of PS-TiO₂-GO composites. PS-ZnO-GO composites too underwent photo-oxidation upon UV irradiation. The only difference was in the extent of photo-oxidation of the composites which was more pronounced in PS-TiO₂-GO compared to that of PS-ZnO-GO. PS-ZnO-GO underwent better photo-oxidation as compared to PS-ZnO composites. The order of photo-oxidation among PS-ZnO-GO composites was as follows: PS-(ZnO-10% GO) > PS-(ZnO-30% GO) > PS-(ZnO-3% GO). Maximum photo-oxidation

among the PS-ZnO-GO composites was exhibited by PS-(ZnO-10% GO). Excess of GO in PS-(ZnO-30% GO) composite might have hampered the rate of photo-oxidation. This irregular trend could be explained by the aggregation of ZnO-GO composites due to the uneven distribution of GO and ZnO in the composites which increased as the percentage of GO increased. Figure 5.9.3 and 5.9.4 represents the FTIR spectra of PS-(ZnO-10%GO) and PS-(ZnO-30%GO) respectively.
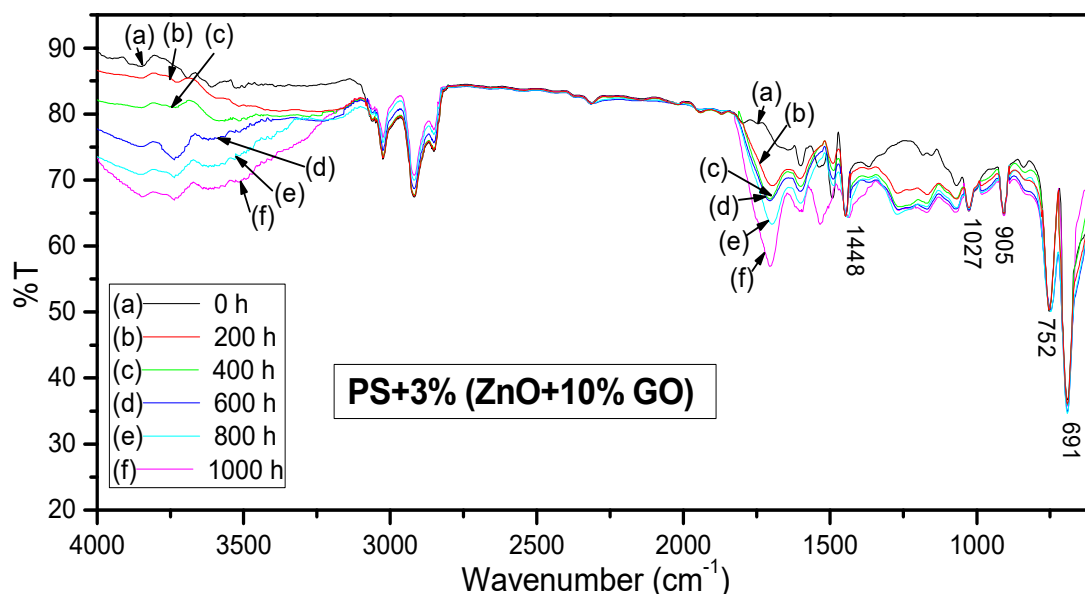

Figure 5.9.3. *FTIR spectra of PS-3%(ZnO-10% GO) after different UV exposure time intervals ranging from 0 h to 1000 h.*
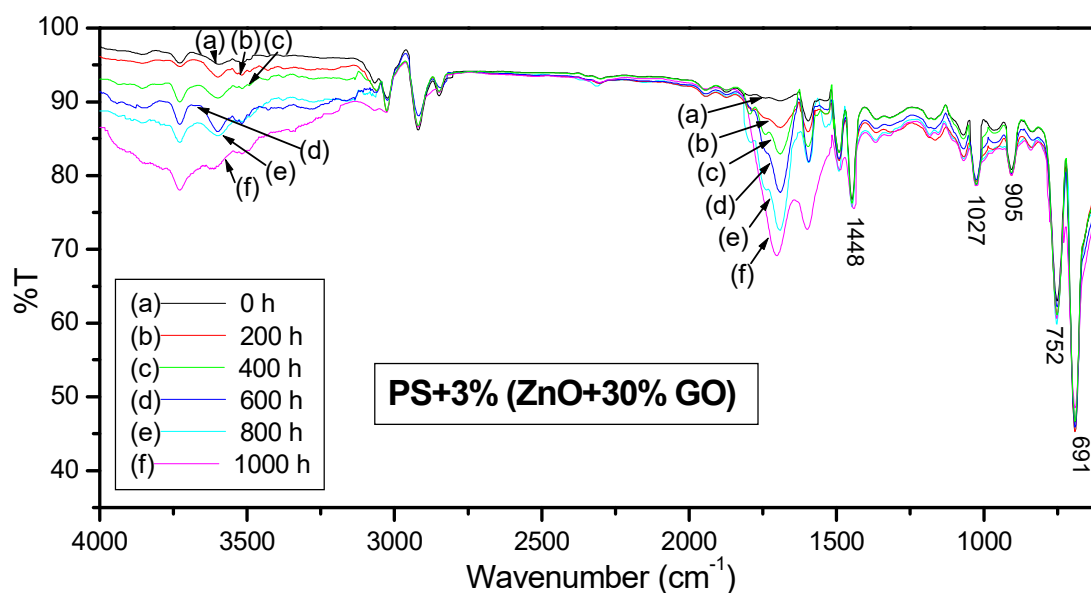

Figure 5.9.4. *FTIR spectra of PS-3%(ZnO-30% GO) after different UV exposure time intervals ranging from 0 h to 1000 h.*

The absorption bands at 691 cm^{-1}, 752 cm^{-1}, 905 cm^{-1} and 1027 cm^{-1} representing phenylic -C-H out of plane bending did not show changes in their intensity in both PS-TiO$_2$-GO and PS-ZnO-GO composites. The peak at 1448 cm^{-1} corresponding to aromatic carbon-carbon double bond stretch also exhibited no change in peak intensity. This could be due to the fact that the phenyl group may have remained intact upon UV irradiation of 1000 hours.

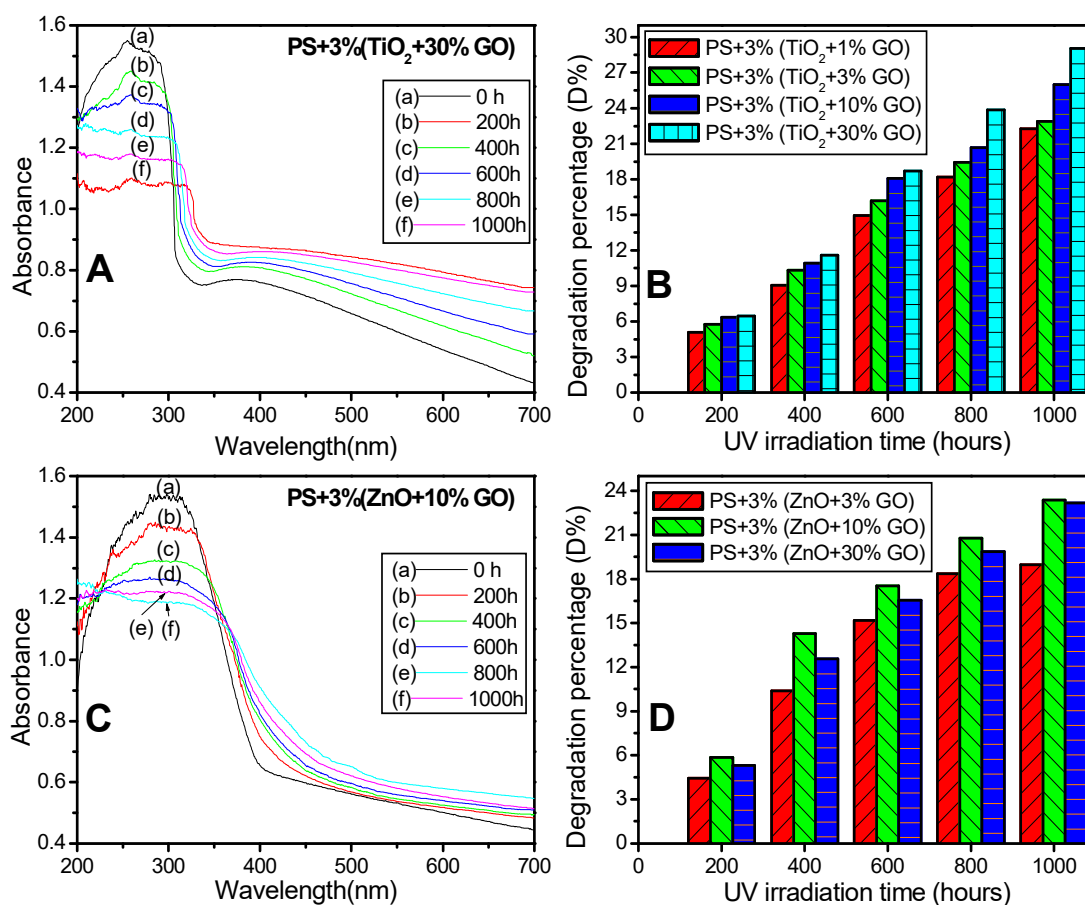### 5.4.3. UV-visible Diffused reflectance spectroscopy (UV-DRS)

Figure 5.10.1. *UV-DRS of PS-3%(TiO$_2$-30% GO) (A), PS-3%(ZnO-10% GO) (C) and degradation percentages of PS-TiO$_2$-GO (B), PS-ZnO-GO (D) composites at different UV exposure time intervals ranging from 0 h to 1000 h*

Both PS-TiO$_2$-GO and PS-ZnO-GO absorbed in the UV as well as in the visible region of spectra as evident from their UV-DRS. Maximum absorption was observed in the UV region of the spectra for all the composites. The absorption in the UV region decreased as the time of UV irradiation increased. Maximum decrease in the UV absorption bands was observed in PS-(TiO$_2$-30%GO) among PS-TiO$_2$-GO

composites (Figure 5.10.1 A). PS-(ZnO-10%GO) underwent maximum decrease in UV absorption among the PS-ZnO-GO composites (Figure 5.10.1 D). A red shift was observed with a slight increase in the absorption bands in visible region for the composites, with an increase in UV exposure time. Degradation percentage determined from UV-DRS of PS-TiO$_2$-GO as well as PS-ZnO-GO are represented in Figure 5.10.1 B and Figure 5.10.1 D respectively. The degradation efficiency of PS-(TiO$_2$-3% GO), PS-(TiO$_2$-10% GO) and PS-(TiO$_2$-30% GO) increased by 13.24, 16.38 and 19.4 % and that of PS-(ZnO-3% GO), PS-(ZnO-10% GO) and PS-(ZnO-30% GO) increased by 9.35, 13.74 and 13.54 % respectively with respect to pristine PS.

Optical bandgap energy (E$_g$) of PS-TiO$_2$-GO and PS-ZnO-GO films before and after UV irradiations at different time intervals was determined using Tauc relation. The values of E$_g$ decreased towards lower energy with respect to UV exposure time of the composites. Figure 5.10.2 represents the direct E$_g$ determination of PS-(TiO$_2$-30% GO) and PS-(ZnO-10% GO) composites by plotting $(\alpha h\upsilon)^2$ versus $h\upsilon$ and extrapolating the linear portion of the curve towards energy ($h\upsilon$) axis. The decrease in E$_g$ could be due to the formation of conjugated double bonds or other species that can absorb the visible light. Degradation of PS chain, leading to the decrease in characteristic UV absorption of PS composites upon UV irradiation also plays a vital role in the decrease of E$_g$ of the composites.
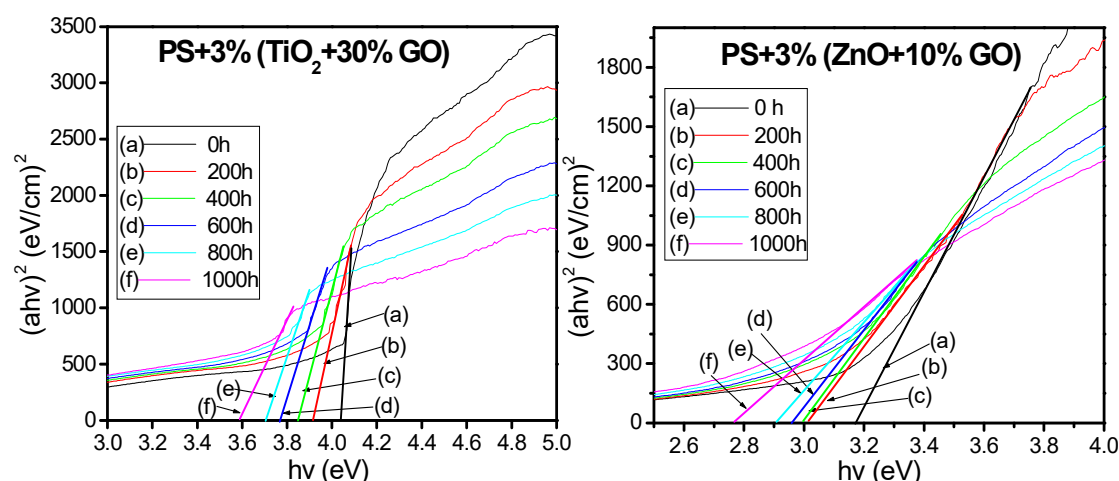

Figure 5.10.2*. Optical bandgap energy determination from the plot of $(\alpha h\upsilon)^2$ v/s $h\upsilon$ for PS-3%(TiO$_2$-30% GO) (A) and PS-3%(ZnO-10% GO) (C) composites subjected to different UV exposure time intervals ranging from 0 h to 1000 h*
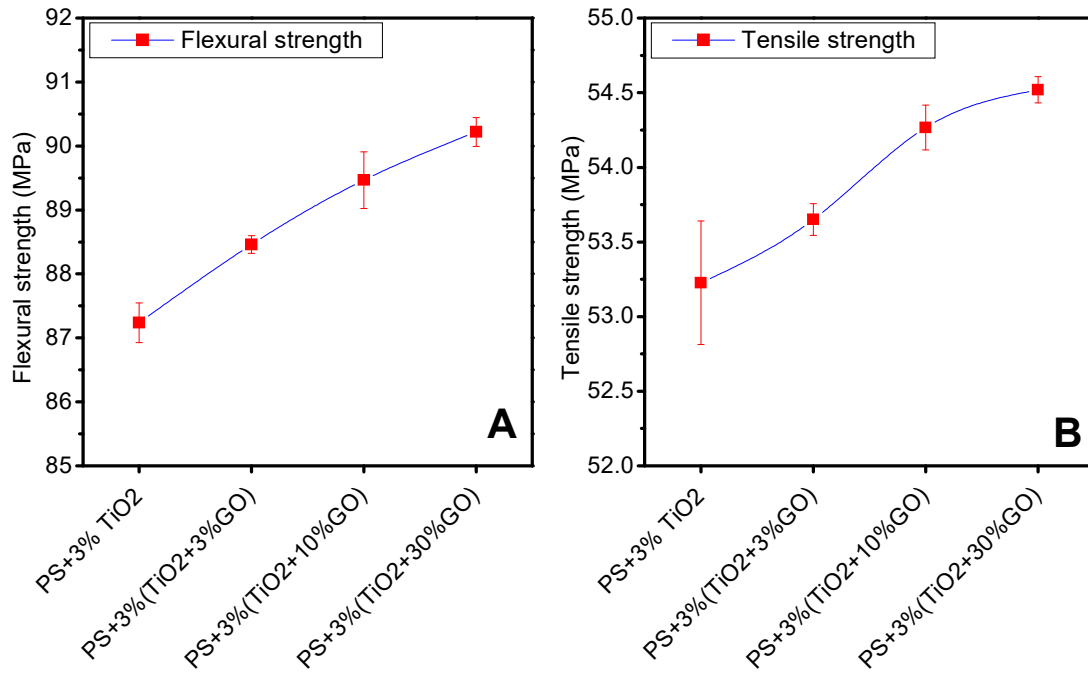
5.4.4. Mechanical Properties

Figure 5.11.1. *Flexural (A) and tensile (B) strengths of PS-TiO₂-GO composites before UV irradiation- a comparison*
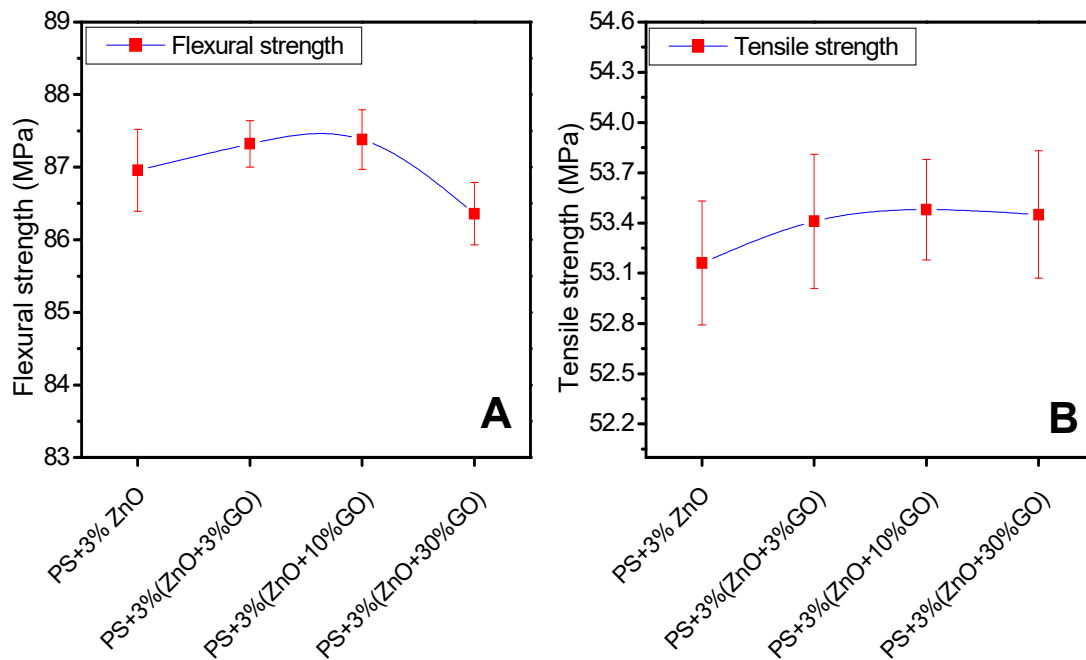

Figure 5.11.2. *Flexural (A) and tensile (B) strengths of PS-ZnO-GO composites before UV irradiation-a comparison*

The flexural and tensile strengths of non-irradiated PS-TiO$_2$-GO composites were greater than that of PS-TiO$_2$ composites (Figure 5.11.1). It was also found that the mechanical strength of the composites increased as the percentage of GO in the composites increased. Maximum flexural and tensile strengths were observed in PS-(TiO$_2$-30% GO) compared to the other PS-TiO$_2$-GO composites. This enhanced mechanical property of PS-TiO$_2$-GO composites promises their application in such devices or commodities where better mechanical strength is in demand.

The flexural and tensile strengths of PS-ZnO-GO composites were better compared to PS-ZnO composite (Figure 5.11.2). In the present study, maximum mechanical strength was observed in PS-(ZnO-10% GO) among the PS-ZnO-GO composites. The mechanical strength of PS-(ZnO-10% GO) was even greater than PS-(ZnO-30% GO).

Comparing Figures 5.11.1 and 5.11.2, it was observed that mechanical strengths of PS-TiO$_2$-GO composites were better than that of PS-ZnO-GO composites. This fact could be explained on the basis of poor distribution of ZnO-GO compared to that of TiO$_2$-GO along the PS matrix. It could be visualized from the SEM and HRTEM images discussed in previous section that ZnO-GO existed as small aggregates while TiO$_2$-GO existed as dispersed nanostructures. The existence of nano sized TiO$_2$ in TiO$_2$-GO composites provided better surface area for associating with GO, breaking them apart into nanosheets. The growth of ZnO particles to bigger rod shaped structures in ZnO-GO composites, on the other hand, provided comparatively lesser surface area for GO association. The GO which remained unassociated with ZnO existed as aggregates as observed in SEM and HRTEM images. Loading PS with ZnO-GO hence resulted in composites with comparatively lower mechanical strength compared to PS loaded with TiO$_2$-GO.

The flexural (Figure 5.11.3) and tensile (Figure 5.11.4) strengths of PS-TiO$_2$-GO and PS-ZnO-GO composites decreased as the time of UV irradiation increased. PS-TiO$_2$-GO composites underwent better decrease in the mechanical properties compared to PS-ZnO-GO composites upon UV irradiation. PS-(TiO$_2$-30% GO) composite underwent maximum decrease in mechanical properties among the PS-TiO$_2$-GO composites. PS-(ZnO-10% GO) showed maximum decrease in the mechanical properties among the PS-ZnO-GO composites.
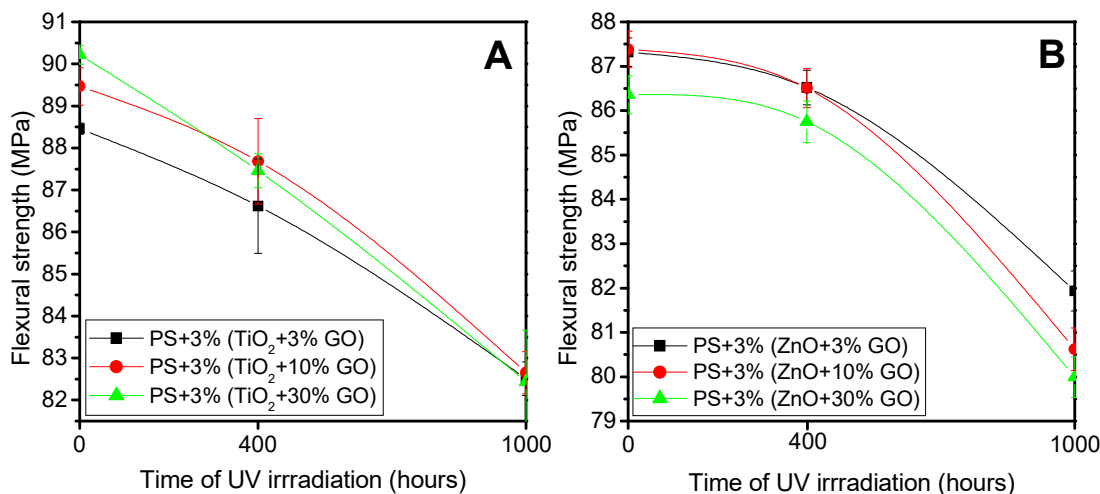
Figure 5.11.3. *Flexural strength of A) PS-TiO$_2$-GO and B) PS-ZnO-GO composites exposed to UV radiation for 0, 400 and 1000 h.*
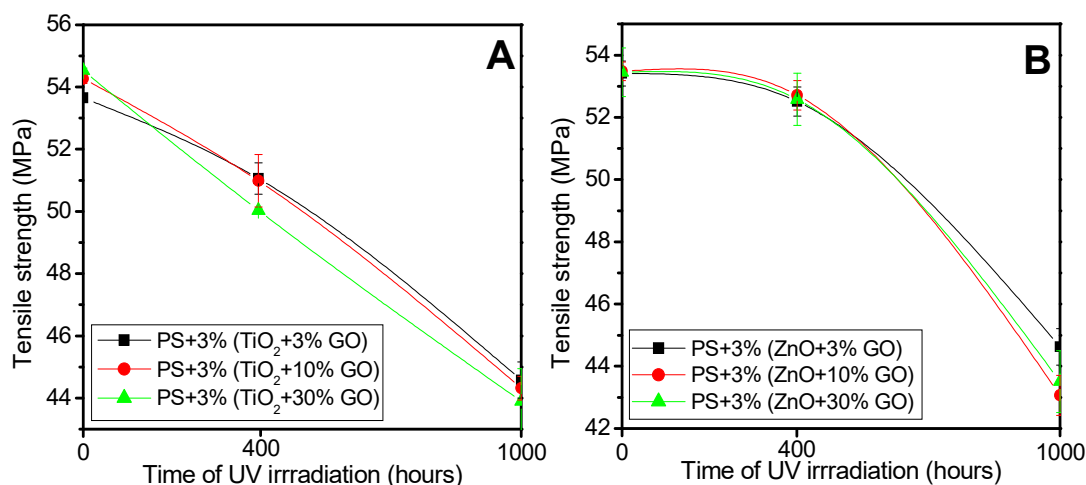

Figure 5.11.4. *Tensile strengts A) PS-TiO$_2$-GO and B) PS-ZnO-GO composites exposed to UV radiation for 0, 400 and 1000 h.*

5.4.5. Electrical properties

Dielectric breakdown (BDV) of PS-TiO$_2$-GO and PS-ZnO-GO composites was lower compared to PS-TiO$_2$ and PS-ZnO composites respectively. BDV of the composites decreased as the percentage of GO in the composites increased (Figure 5.12.1). The presence of conducting GO in the composites might have resulted in the easy passage of electric current leading to easier breakdown of the composites. BDV of the composites decreased with the increase in UV irradiation time (Figure 5.12.1). The formation of charged centers with better mobility through the composites on UV irradiation was hence evident. BDV of PS-(TiO$_2$-30% GO) decreased to a greater

extent among the PS-TiO$_2$-GO composites with the increase in UV irradiation time. PS-(ZnO-10% GO) composite showed better decrease in BDV among the PS-ZnO-GO composites upon UV irradiation.
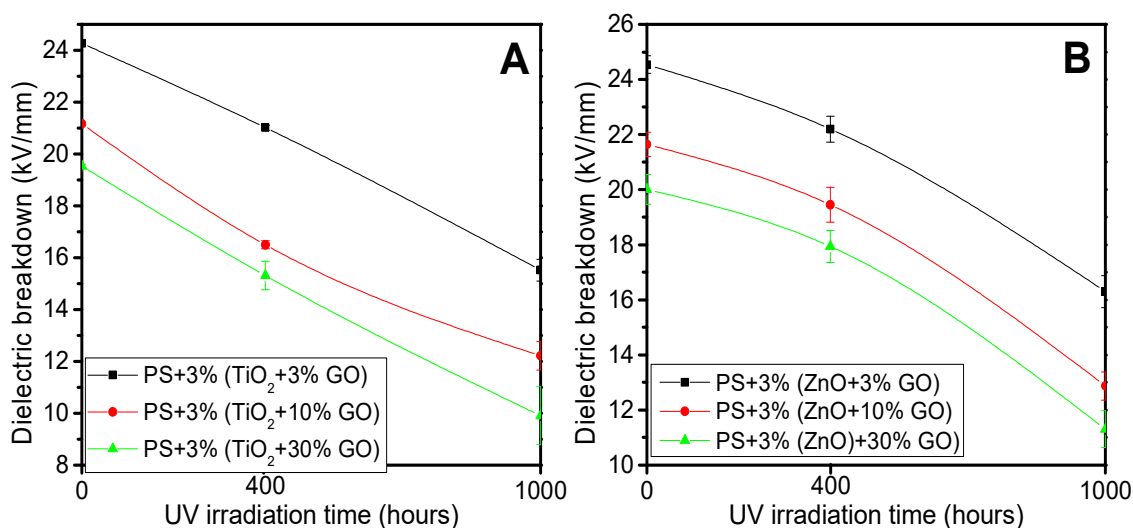

Figure 5.12.1. *Dielectric breakdown of PS-TiO$_2$-GO and PS-ZnO-GO composites exposed to UV radiation for 0, 400 and 1000 h.*

Dielectric permittivity (ε_r) of the composites increased as the time of UV irradiation increased. Figure 5.12.2 represents the dielectric permittivity of PS-(TiO$_2$-30% GO) and PS-(ZnO -30% GO) composites with UV exposure intervals of 0, 400 and 1000 hours respectively. In both the composites, ε_r increased as the time of UV irradiation increased.
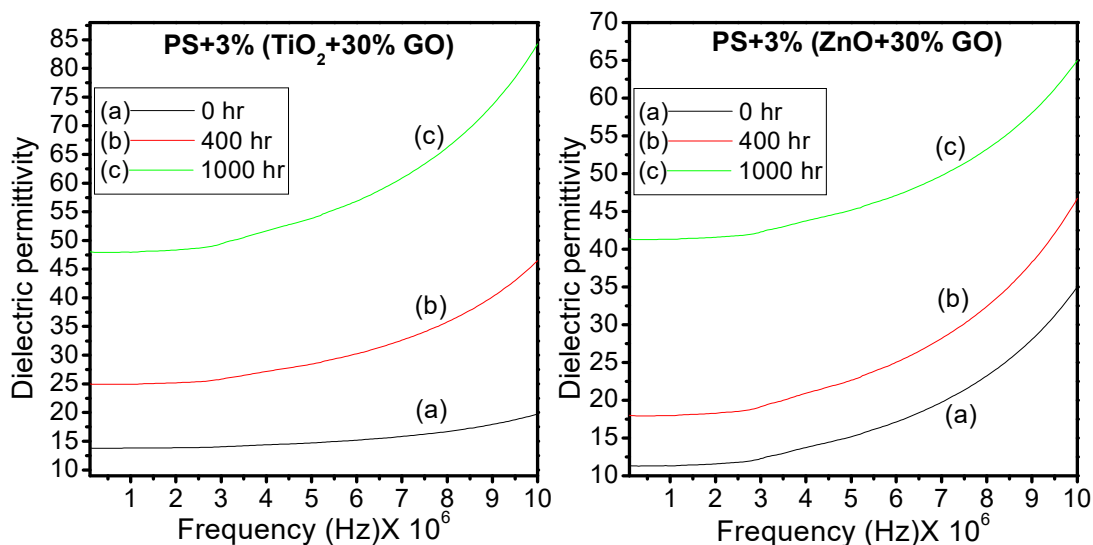

Figure 5.12.2. *Dielectric permittivity of PS-(TiO$_2$-30%GO) and PS-(ZnO-30%GO) composites exposed to UV radiation for 0, 400 and 1000 h.*

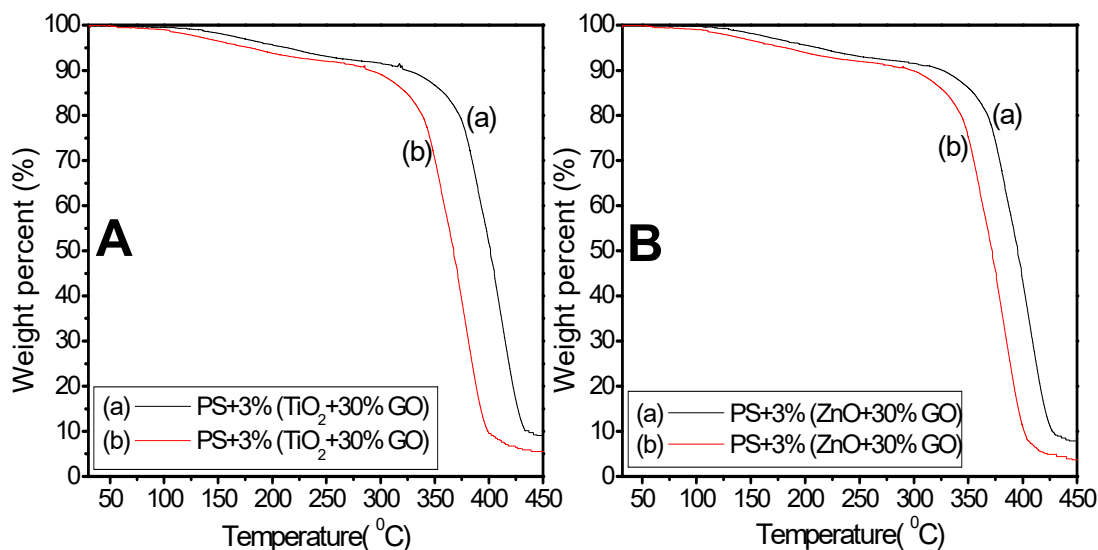### 5.4.6. Thermogravimetric Analysis (TGA)

Figure 5.13. *TGA thermogram of PS-3% (TiO₂+30% GO) (A) and PS-3%*
(ZnO+30% GO) (B) composites before and after UV irradiation of 1000 h

TGA thermograms of PS-(TiO$_2$-30% GO) and PS-(ZnO-30% GO) conducted under nitrogen atmosphere as represented in figure 5.13, displayed two stages of weight loss. The first stage of weight loss represents water desorption and the second stage represent decomposition of the polymer composites. The decomposition temperature of PS-(TiO$_2$-30% GO) ranged between 320-434°C before UV irradiation (Figure 5.13 A). The decomposition temperature of PS-(ZnO-30% GO) before UV irradiation was between 314-429°C respectively (Figure 5.13 B). The decomposition temperatures of the composites decreased with the increase in UV exposure time. The decomposition temperature of PS-(TiO$_2$-30% GO) decreased 872-401°C and that of PS-(ZnO-30% GO) decreased to 292-408°C respectively upon UV irradiation of 1000 hours. Decreased thermal stability of the polymer composites as a result of degradation is evident here.

5.4.7. Weight loss

Weight loss percentage of PS-TiO$_2$-GO and PS-ZnO-GO composites exposed to UV radiation of varying time intervals ranging from 0 to 1000 hours are represented below (Figure 5.14). The percentage of weight loss increased with respect to UV irradiation time. Evolution of volatile species produced during the photodegradation process is evident here. PS-(TiO$_2$-30% GO) underwent maximum weight loss among

PS-TiO$_2$-GO composites and PS-(ZnO-10% GO) underwent maximum weight loss among PS-ZnO-GO composites upon UV irradiation.
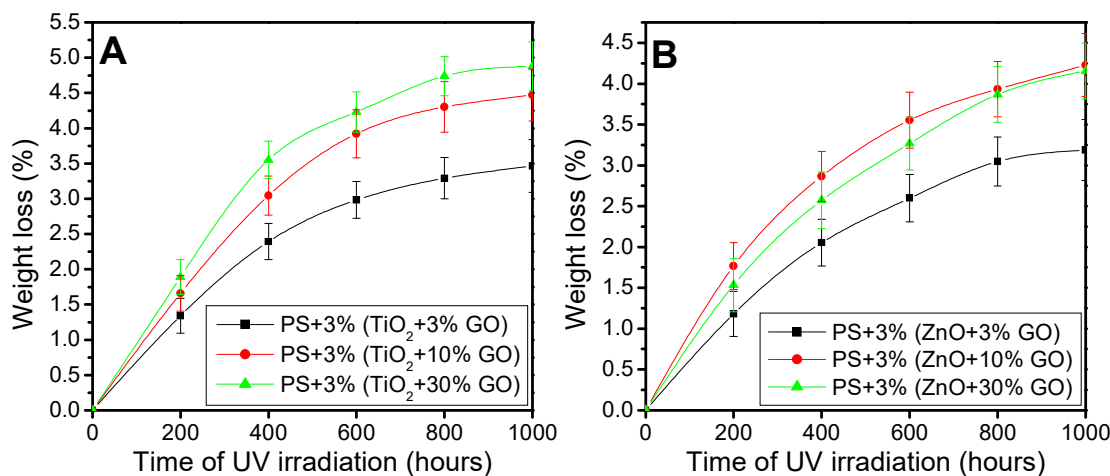

Figure 5.14. *Comparison of weight loss percentages of PS-3%(TiO$_2$- GO) (A) and PS-3%(ZnO-GO)(B) composites at regular intervals of UV irradiation*

5.5. Mechanism of Photodegradation of PS-TiO$_2$-GO/ PS-ZnO-GO composites

It was confirmed from various analytic techniques discussed above that PS-TiO$_2$-GO and PS-ZnO-GO composites underwent better photo-oxidative degradation compared to PS-TiO$_2$ and PS-ZnO composites. In other words, the photocatalytic efficiency of TiO$_2$ and ZnO has been enhanced on coupling them with GO. GO coupled with TiO$_2$ or ZnO reduces the electron–hole recombination upto an appreciable extent. Raman spectroscopy proved the partial reduction of GO (into reduced graphene oxide) in TiO$_2$-GO composites discussed above. The reduced graphene oxide acts as better electron sink. The photogenerated electrons present in the conduction band (CB) of TiO$_2$ or ZnO are transferred into the Fermi levels of carbon atoms of these reduced GO instead minimizing the chance of recombining[35]. These electrons are resonance stabilized in the GO sheet and can recombine with adsorbed oxygen producing various reactive species (like O$^-$, O$_2$•$^-$ etc). These species interact with the PS chain initiating photo-oxidation of the chain. The holes left behind in the VB of TiO$_2$ or ZnO can now combine easily with the adsorbed water or OH$^-$ ions resulting in the formation of OH• which interacts with the PS chain initiating another set of reactions including –OH and –OOH substitution over the chain (Figure 5.15).
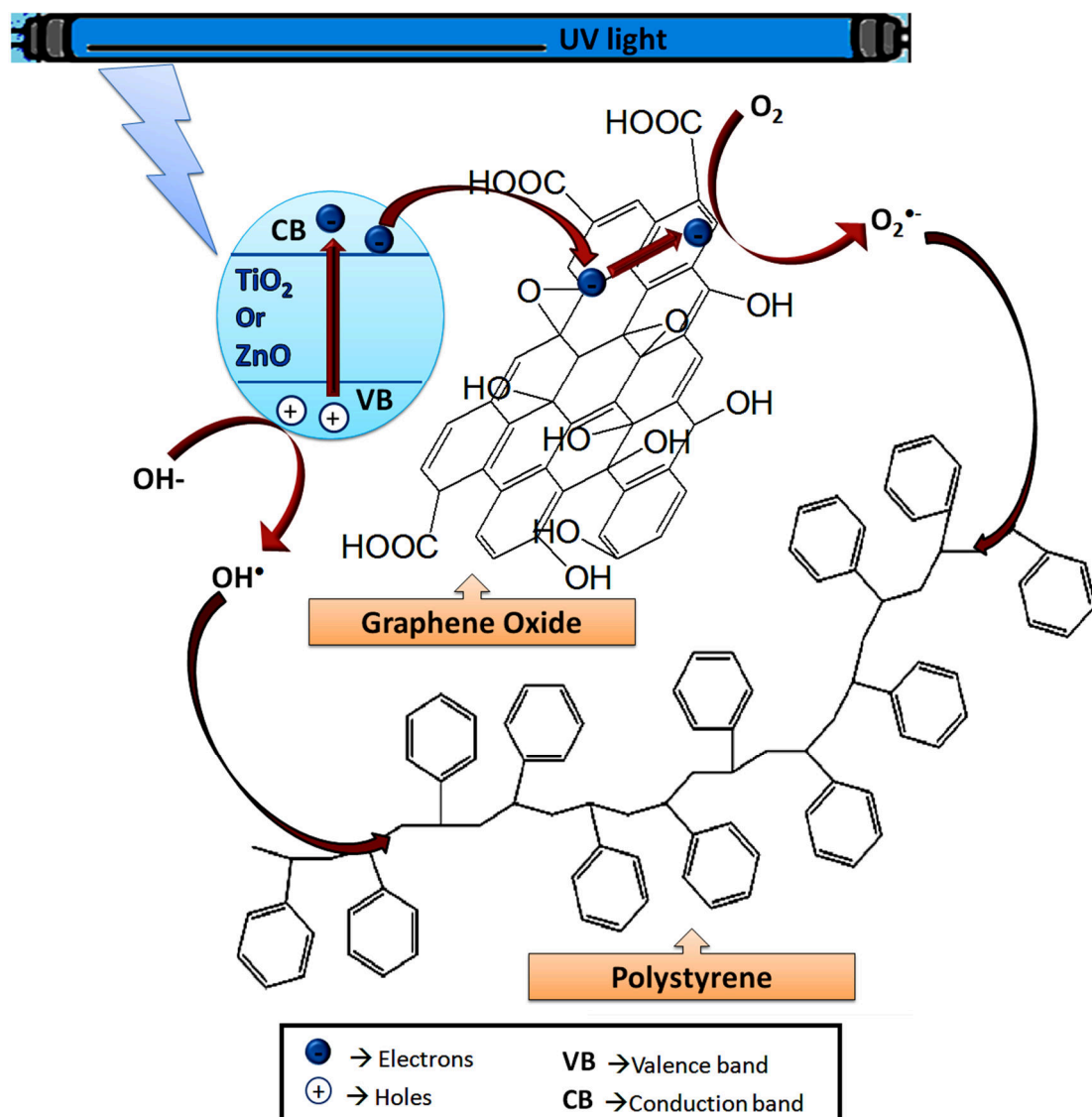
Figure 5.15. *Schematic representation of photodegradation mechanism of PS by TiO₂-GO/ZnO-GO catalysts through charge transfer*

Other than the interfacial charge transfer occurring in the heterojunctions of the metal oxides and GO, the formation of Ti-O-C/Zn-O-C and Ti-C bonds act as a bridge for the transport of electrons. The photogenerated electrons transported from the TiO$_2$/ZnO to the carbon atoms of GO are highly stabilized and hence the chance of recombination of the electron-hole pair is minimized.

5.6. Conclusions

GO could be successfully prepared from graphite through chemical oxidation approach following ultrasonication assisted modified Hummer's method. TiO$_2$-GO and ZnO-GO composites were prepared through ultrasonication assisted hydrothermal

method. Preparation of TiO_2-GO resulted in nano sized separated crystalline particles whereas ZnO-GO were aggregated. Photodegradation of PS in the presence of TiO_2-GO and ZnO-GO composites as photocatalysts were studied. Both PS-TiO_2-GO and PS-ZnO-GO underwent photo-oxidative degradation in the presence of UV radiation. They also underwent polymer chain scission upon UV irradiation. The composites underwent better photodegradation compared to PS-TiO_2 as well as PS-ZnO composites. Mechanical properties of the composites were enhanced in PS-TiO_2-GO and PS-ZnO-GO composites compared to PS-TiO_2 and PS-ZnO composites. Possible application of the composites, where better mechanical strength is in demand, is hence promised. The mechanical strength of the composites decreased when subjected to UV irradiation. The value of BDV of the composites was lower than that of PS-TiO_2, PS-ZnO and even PS. The possibility for the application of the composites, where better conductivity is required, can hence be assured. BDV of the composites decreased upon UV irradiation. Formation of charged species as a consequence of photodegradation was hence evident. Dielectric permittivity of the composites increased upon UV irradiation due to the formation of charged dipoles. The thermal stability of the composites too decreased as a consequence of photodegradation as evident from TGA. It can be concluded that the photocatalytic efficiency of TiO_2 and ZnO was enhanced upon coupling with GO. The possibility of various interactions including hydrogen bond and Ti-O-C/Zn-O-C bond formation between TiO_2/ZnO and GO could have assisted the intrafacial charge transfer between the heterojunctions of TiO_2/ZnO and GO. The photogenerated electrons can transfer from the conduction bands of TiO_2/ZnO into Fermi levels of GO. This appreciably decreases the electron-hole recombination possibility within TiO_2 or ZnO. The resonance stabilized electrons delocalized in the π bonds of GO can interact with oxygen atoms in the atmosphere leading to reactive species that could initiate the photodegradation of PS chain. The holes left behind in the valence band of TiO_2/ZnO could further combine with the adsorbed water molecules or OH^- ions resulting in OH• that can interact with PS chain resulting in its degradation. PS-TiO_2-GO composites underwent better photo-oxidative degradation compared to PS-ZnO-GO composites. PS-(TiO_2-30% GO) exhibits maximum photodegradation among PS-TiO_2-GO composites and PS-(ZnO-10% GO) exhibits maximum photodegradation among PS-ZnO-GO composites.

References

1. Girishkumar, G., Vinodgopal, K. & Kamat, P. V. Carbon Nanostructures in Portable Fuel Cells: Single-Walled Carbon Nanotube Electrodes for Methanol Oxidation and Oxygen Reduction. *J. Phys. Chem. B* **108**, 19960–19966 (2004).
2. Brown, P., Takechi, K. & Kamat, P. V. Single-Walled Carbon Nanotube Scaffolds for Dye-Sensitized Solar Cells. *J. Phys. Chem. C* **112**, 4776–4782 (2008).
3. Eckert, J.-F. *et al.* Fullerene−Oligophenylenevinylene Hybrids: Synthesis, Electronic Properties, and Incorporation in Photovoltaic Devices. *J. Am. Chem. Soc.* **122**, 7467–7479 (2000).
4. Thomas, K. G., George, M. V & Kamat, P. V. Photoinduced Electron-Transfer Processes in Fullerene-Based Donor–Acceptor Systems. *Helv. Chim. Acta* **88**, 1291–1308 (2005).
5. Iijima, S. Helical microtubules of graphitic carbon. *Nature* **354**, 56–58 (1991).
6. Rao, C. N. R., Sood, A. K., Voggu, R. & Subrahmanyam, K. S. Some Novel Attributes of Graphene. *J. Phys. Chem. Lett.* **1**, 572–580 (2010).
7. Novoselov, K. S. *et al.* Electric Field Effect in Atomically Thin Carbon Films. *Science (80-.).* **306**, 666–669 (2004).
8. Lee, C., Wei, X., Kysar, J. W. & Hone, J. Measurement of the elastic properties and intrinsic strength of monolayer graphene. *Science (80-.).* **321**, 385–388 (2008).
9. Balandin, A. A. *et al.* Superior Thermal Conductivity of Single-Layer Graphene. *Nano Lett.* **8**, 902–907 (2008).
10. Huang, X., Qi, X., Boey, F. & Zhang, H. Graphene-based composites. *Chem. Soc. Rev.* **41**, 666–686 (2012).
11. Singh, E. & Nalwa, H. S. Stability of graphene-based heterojunction solar cells. *RSC Adv.* **5**, 73575–73600 (2015).
12. Stankovich, S. *et al.* Graphene-based composite materials. *Nature* **442**, 282–286 (2006).
13. Jasuja, K. & Berry, V. Implantation and Growth of Dendritic Gold Nanostructures on Graphene Derivatives: Electrical Property Tailoring and Raman Enhancement. *ACS Nano* **3**, 2358–2366 (2009).
14. Wang, X., Zhi, L. & Müllen, K. Transparent, Conductive Graphene Electrodes for Dye-Sensitized Solar Cells. *Nano Lett.* **8**, 323–327 (2008).
15. Stoller, M. D., Park, S., Zhu, Y., An, J. & Ruoff, R. S. Graphene-based ultracapacitors. *Nano Lett.* **8**, 3498–3502 (2008).
16. Liu, Z., Robinson, J. T., Sun, X. & Dai, H. PEGylated Nanographene Oxide for Delivery of Water-Insoluble Cancer Drugs. *J. Am. Chem. Soc.* **130**, 10876–10877 (2008).
17. Liu, Z., Tabakman, S., Welsher, K. & Dai, H. Carbon nanotubes in biology and medicine: in vitro and in vivo detection, imaging and drug delivery. *Nano Res.* **2**, 85–120 (2009).
18. Robinson, J. T., Perkins, F. K., Snow, E. S., Wei, Z. & Sheehan, P. E. Reduced graphene oxide molecular sensors. *Nano Lett.* **8**, 3137–3140 (2008).
19. Park, S. & Ruoff, R. S. Chemical methods for the production of graphenes. *Nat. Nanotechnol.* **4**, 217–224 (2009).
20. He, H., Riedl, T., Lerf, A. & Klinowski, J. Solid-State NMR Studies of the Structure of Graphite Oxide. *J. Phys. Chem.* **100**, 19954–19958 (1996).
21. He, H., Klinowski, J., Forster, M. & Lerf, A. A new structural model for graphite oxide. *Chem. Phys. Lett.* **287**, 53–56 (1998).
22. Lerf, A., He, H., Forster, M. & Klinowski, J. Structure of Graphite Oxide Revisited. *J. Phys. Chem. B* **102**, 4477–4482 (1998).
23. Cai, W. *et al.* Synthesis and Solid-State NMR Structural Characterization of 13C-Labeled Graphite Oxide. *Science (80-.).* **321**, 1815–1817 (2008).
24. Dreyer, D. R., Park, S., Bielawski, C. W. & Ruoff, R. S. The chemistry of graphene oxide. *Chem. Soc. Rev.* **39**, 228–240 (2010).
25. Kamat, P. V. Graphene-Based Nanoarchitectures. Anchoring Semiconductor and Metal Nanoparticles on a Two-Dimensional Carbon Support. 520–527 (2010). doi:10.1021/jz900265j
26. Naknikham, U. *et al.* Mutual-stabilization in chemically bonded graphene oxide–TiO2

heterostructures synthesized by a sol–gel approach. *RSC Adv.* **7**, 41217–41227 (2017).

27. Williams, G., Seger, B. & Kamat, P. V. TiO2-Graphene Nanocomposites. UV-Assisted Photocatalytic Reduction of Graphene Oxide. *ACS Nano* **2**, 1487–1491 (2008).

28. Kumar, A., Bansal, A., Behera, B., Jain, S. L. & Ray, S. S. Ternary hybrid polymeric nanocomposites through grafting of polystyrene on graphene oxide-TiO2 by surface initiated atom transfer radical polymerization (SI-ATRP). *Mater. Chem. Phys.* **172**, 189–196 (2016).

29. Huang, Q. *et al.* Enhanced Photocatalytic Activity of Chemically Bonded TiO2/Graphene Composites Based on the Effective Interfacial Charge Transfer through the C–Ti Bond. *ACS Catal.* **3**, 1477–1485 (2013).

30. He, D., Li, Y., Wang, J., Yang, Y. & An, and Q. Tunable Nanostructure of TiO$_2$/Reduced Graphene Oxide Composite for High Photocatalysis. *Appl. Microsc.* **46**, 37–44 (2016).

31. Gillespie, P. N. O. & Martsinovich, N. Origin of Charge Trapping in TiO2/Reduced Graphene Oxide Photocatalytic Composites: Insights from Theory. *ACS Appl. Mater. Interfaces* **11**, 31909–31922 (2019).

32. Benjwal, P., Kumar, M., Chamoli, P. & Kar, K. Enhanced photocatalytic degradation of methylene blue and adsorption of arsenic(III) by reduced graphene oxide (rGO)–metal oxide (TiO2/Fe3O4) based nanocomposites. *RSC Adv.* **5**, 73249–73260 (2015).

33. Umrao, S. *et al.* A possible mechanism for the emergence of an additional bandgap due to a Ti–O–C bond in the TiO2–graphene hybrid system for enhanced photodegradation of methylene blue under visible light. *RSC Adv.* **4**, 59890–59901 (2014).

34. Djellabi, R., Yang, B., Wang, Y., Cui, X. & Zhao, X. Carbonaceous biomass-titania composites with TiOC bonding bridge for efficient photocatalytic reduction of Cr(VI) under narrow visible light. *Chem. Eng. J.* **366**, 172–180 (2019).

35. Tang, B., Chen, H., Peng, H., Wang, Z. & Huang, W. Graphene Modified TiO$_2$ Composite Photocatalysts: Mechanism, Progress and Perspective. *Nanomater. (Basel, Switzerland)* **8**, (2018).

36. Rakkesh, R. A., Durgalakshmi, D. & Balakumar, S. Efficient sunlight-driven photocatalytic activity of chemically bonded GNS–TiO2 and GNS–ZnO heterostructures. *J. Mater. Chem. C* **2**, 6827–6834 (2014).

37. Liang, Y., Wang, H., Sanchez Casalongue, H., Chen, Z. & Dai, H. TiO2 nanocrystals grown on graphene as advanced photocatalytic hybrid materials. *Nano Res.* **3**, 701–705 (2010).

38. Hummers, W. S. & Offeman, R. E. Preparation of Graphitic Oxide. *J. Am. Chem. Soc.* **80**, 1339 (1958).

39. Sreekanth, T. V. M., Jung, M.-J. & Eom, I.-Y. Green synthesis of silver nanoparticles, decorated on graphene oxide nanosheets and their catalytic activity. *Appl. Surf. Sci.* **361**, 102–106 (2016).

40. Marcano, D. C. *et al.* Improved Synthesis of Graphene Oxide. *ACS Nano* **4**, 4806–4814 (2010).

41. Dimiev, A. M. & Tour, J. M. Mechanism of Graphene Oxide Formation. *ACS Nano* **8**, 3060–3068 (2014).

42. Lowe, S. & Zhong, Y. L. Challenges of Industrial-Scale Graphene Oxide Production: Fundamentals and Applications. in *Graphene Oxide: Fundamentals and Applications* 410–431 (2016). doi:10.1002/9781119069447.ch13

43. Paulchamy, B., Arthi, G. & Lignesh, B. D. A simple approach to stepwise synthesis of graphene oxide nanomaterial. *J Nanomed Nanotechnol* **6**, 1 (2015).

44. Gao, P., Li, A., Sun, D. D. & Ng, W. J. Effects of various TiO2 nanostructures and graphene oxide on photocatalytic activity of TiO2. *J. Hazard. Mater.* **279**, 96–104 (2014).

45. Rong, X. *et al.* Preparation , characterization and photocatalytic application of TiO 2 – graphene photocatalyst under visible light irradiation. *Ceram. Int.* 1–10 (2014). doi:10.1016/j.ceramint.2014.10.072

46. Perera, S. D. *et al.* Hydrothermal Synthesis of Graphene-TiO2 Nanotube Composites with Enhanced Photocatalytic Activity. *ACS Catal.* **2**, 949–956 (2012).

47. Ameen, S., Akhtar], M. [Shaheer, Seo, H.-K. & Shin], H. [Shik. Advanced ZnO–graphene oxide nanohybrid and its photocatalytic Applications. *Mater. Lett.* **100**, 261–265 (2013).

48. Lee, K. S., Park, C. W., Lee, S. J. & Kim, J.-D. Hierarchical zinc oxide/graphene oxide composites for energy storage devices. *J. Alloys Compd.* **739**, 522–528 (2018).

49. Arami, H., Mazloumi, M., Khalifehzadeh, R. & Sadrnezhaad, S. K. Sonochemical preparation of TiO2 nanoparticles. *Mater. Lett.* **61**, 4559–4561 (2007).

50. Zhang, Y., Tang, Z.-R., Fu, X. & Xu, Y.-J. Engineering the Unique 2D Mat of Graphene to Achieve Graphene-TiO2 Nanocomposite for Photocatalytic Selective Transformation: What Advantage does Graphene Have over Its Forebear Carbon Nanotube? *ACS Nano* **5**, 7426–7435 (2011).

51. Štengl, V., Bakardjieva, S., Grygar, T. M., Bludská, J. & Kormunda, M. TiO 2-graphene oxide nanocomposite as advanced photocatalytic materials. *Chem. Cent. J.* **7**, 41 (2013).

52. Zhang, H., Lv, X., Li, Y., Wang, Y. & Li, J. P25-graphene composite as a high performance photocatalyst. *ACS Nano* **4**, 380–386 (2009).

53. Liu, H. *et al.* A green and direct synthesis of graphene oxide encapsulated TiO2 core/shell structures with enhanced photoactivity. *Chem. Eng. J.* **230**, 279–285 (2013).

54. Khannam, M., Sharma, S., Dolui, S. & Dolui, S. K. A graphene oxide incorporated TiO2 photoanode for high efficiency quasi solid state dye sensitized solar cells based on a poly-vinyl alcohol gel electrolyte. *RSC Adv.* **6**, 55406–55414 (2016).